

ABSTRACT

IMAGE SEGMENTATION AND PAIRED SHAPES ASYMMETRY  
QUANTIFICATION: AN APPLICATION IN A  
DROSOPHILA WING IMAGE SET

By

G.D. Young

May 2015

The current process to identify wing pair shape asymmetry in *Drosophila* wing images contains multiple layers of potential measurement error. The image segmentation routine is a low-level method performed on a low resolution image set, and is prone to inaccurate edge detection in finding the wing's interior vascular structure and the exterior wing edge. An automated splining procedure on the segmentation result which yields the locations of several landmark points on the wing itself has several erroneous spline control points. The process to correct errors in the data requires both parameter tuning in the algorithm as well as manual correction of the segmentation and splining results. The in-production measures of asymmetry between *Drosophila* wing pairs are shown to be sensitive to these measurement errors. To reduce error in the segmentation step, several image segmentation methods are analyzed for use in developing a robust, efficient and automated segmentation algorithm for *Drosophila* wing image sets. Evaluation of the accuracy and efficiency of the methods is discussed, with a focus on the performance of multi-scale methods. A Frangi multi-scale segmentation is shown to more accurately locate the wing's interior vascular network. Additionally, an alternative principal components analysis of the variance structure in the image set is developed to isolate and quantify wing pair shape variation across the data set. This analysis replaces the splining process to identify

locations of landmark points. Alternative measures of wing pair shape asymmetry are created from this analysis and an alternative measure of Directional Asymmetry (DA) is shown to reproduce existing benchmark measures of DA.

IMAGE SEGMENTATION AND PAIRED SHAPES ASYMMETRY  
QUANTIFICATION: AN APPLICATION IN A  
DROSOPHILA WING IMAGE SET

A THESIS

Presented to the Department of Mathematics and Statistics  
California State University, Long Beach

In Partial Fulfillment  
of the Requirements for the Degree  
Master of Science in Applied Mathematics

Committee Members:

William Ziemer, Ph.D.  
Jen-Mei Chang, Ph.D.  
Ashley Carter, Ph.D.

College Designee:

Tangan Gao, Ph.D.

By G.D. Young

B.S., Economics, 1995, The University of Chicago

May 2015

UMI Number: 1589666

All rights reserved

INFORMATION TO ALL USERS

The quality of this reproduction is dependent upon the quality of the copy submitted.

In the unlikely event that the author did not send a complete manuscript and there are missing pages, these will be noted. Also, if material had to be removed, a note will indicate the deletion.



UMI 1589666

Published by ProQuest LLC (2015). Copyright in the Dissertation held by the Author.

Microform Edition © ProQuest LLC.

All rights reserved. This work is protected against unauthorized copying under Title 17, United States Code



ProQuest LLC.  
789 East Eisenhower Parkway  
P.O. Box 1346  
Ann Arbor, MI 48106 - 1346

## TABLE OF CONTENTS

	Page
LIST OF TABLES .....	iii
LIST OF FIGURES .....	iv
CHAPTER	
1. INTRODUCTION .....	1
2. IMAGE PROCESSING AND DATA SET DETAILS .....	4
Image Processing Basics .....	4
Image Data Set .....	5
3. ADAPTIVE THRESHOLDING METHOD .....	9
Overview .....	9
Adaptive Histogram Feature Analysis .....	10
Algorithm Methodology .....	11
Results .....	14
4. MAXIMAL GRADIENT SEGMENTATION .....	15
Gradient Segmentation Overview .....	15
Mathematics .....	15
Strong and Weak Edges .....	17
Algorithm .....	19
Result .....	21
5. FRANGI MULTI-SCALE SEGMENTATION .....	23
Scale Space .....	23
Multi-Scale Segmentation .....	24
Mathematics .....	25
Sharpening Preprocessing .....	28
Frangi Segmentation .....	29
Results .....	32
6. IMAGE SEGMENTATION SUMMARY .....	35
7. PROPOSED MEASURE OF WING PAIR SHAPE ASYMMETRY ...	40
Introduction .....	40
Background Math: Singular Value Decomposition .....	43
Isolation of Wing Shape Variation .....	45
Low-Rank Approximations .....	48
Comparison of the Directional Asymmetry Measures .....	53
Further Work .....	60
Summary .....	61

	Page
APPENDICES .....	64
A. MATLAB CODES .....	65
BIBLIOGRAPHY .....	71

## LIST OF TABLES

TABLE		Page
1	Frangi 2d Pixel Classification Heuristic .....	30
2	Segmentation Methods Performance Comparison .....	36
3	The Benchmark Wingpair Asymmetry Measures Rankings .....	41
4	Rankings of a New Measure of Wingpair Directional Asymmetry .....	51
5	Rankings of a New Measure of Wingpair Fluctuating Asymmetry.....	52
6	Evolution of Wing As Blob Wing9 Trailing Edge Location.....	59

## LIST OF FIGURES

FIGURE	Page
1 Computer image equivalents. ....	5
2 A representative wing image annotated with key features. ....	6
3 An image’s smoothed pixel intensity value probability distribution. ...	7
4 Issues in segmentation: close-up of wing45BIG trailing edge .....	8
5 Adaptive Thresholding segmentation essential steps. ....	13
6 Example Adaptive Thresholding segmentation result (wing1BIG). ....	14
7 Wing boundary region before and after smoothing. ....	16
8 Gradient quiver plots of a vein region. ....	17
9 Abundance of image gradient in wing images. ....	20
10 Raw Maximal Gradient output on wing3BIG .....	21
11 Example Maximal Gradient segmentation result (wing3BIG). ....	22
12 Normal curvature of a space curve .....	27
13 A comparison of the original and sharpened image. ....	29
14 Raw output of the Frangi edge detector. ....	29
15 Frangi segmentation essential steps. ....	32
16 Example Frangi segmentation result (wing45BIG). ....	33
17 Frangi Segmentation leading edge placement. ....	34
18 Frangi segmentation LV V placement. ....	34
19 Annotated segmentation results comparison for wing30BIG. ....	37
20 Original (left) and sharpened wing30BIG image. ....	38
21 Reduction of pose variance through alignment. ....	43
22 Wing As Blob data set singular values plot. ....	46
23 Aligned Wing As Blob wings 1 – 9 .....	47
24 The nine PCs of largest explained variance .....	48

FIGURE	Page
25 Contributions of PCs 1-9 to a low-rank approximation of wing5. ....	49
26 Contributions of PCs 1-9 to a low-rank approximation of wing6. ....	50
27 Scatterplots of WSAI and Unscaled DA z-scores for the 24 flies. ....	54
28 Landmark point location error. ....	56
29 An illustration of the shape effects of PCs of lower explained variance.	59
30 Contributions of the first three PCs to the Wing As Blob wing set. ....	60
31 Wing As Blob wing9 rank 1 approximation southern edge zoom. ....	63

## CHAPTER 1

### INTRODUCTION

Fruit flies (*Drosophila Melanogaster*) have been used as a primary object in the study of genetics and disease for over 100 years. The fruit fly has maintained its status as a primary object of study for many reasons. Multiple generations can be studied in a relatively short amount of time, since a fruit fly lives only ten to eighteen days and a female lays up to 400 eggs in her lifetime [1]. Its genome is well known – in the year 2000 the fruit fly was the first multicellular organism to have its genome fully sequenced. Random genetic mutations in the fruit fly are induced almost at will via radiation exposure. Manipulation of gene expression is relatively straightforward given simpler gene interactions and advanced knowledge of the genome. Finally, understanding fruit fly genetics is believed to lead to better understanding of human disease, since approximately 70% of fruit fly genes have analogues in humans.

Evolutionary geneticists study the heritability of asymmetry in paired biological features. *Directional Asymmetry* (DA) is a measure of mean difference in a population between left and right in a feature pair. DA is of particular interest, since it is the only known trait to exist in nature which cannot be selected for in artificial selection experiments. Generations of photographs of fruit fly wing pairs are the object basis of many of the scientific analyses of asymmetry, since the genome is well known, the wings play an important role in several important behaviors of the fly beyond flight, including courtship and sensing, and images of the wings are easily acquired [2], [3].

The image analysis process begins with an intensity value thresholding-based acquisition of wing data from a low resolution photograph of the fly wing using *WINGMACHINE*. *WINGMACHINE* then fits nine cubic

B-splines to the veins and edges of the *Drosophila* wing given the location points of the humeral break and alula notch and an *a priori* model of general wing shape: see Figure 2 for a wing image annotated with key features, and Houle et al. for a more detailed discussion of the splining procedure [4]. However, due in part to the coarseness of the thresholding-based segmentation, the splining procedure frequently cannot accurately identify the locations of the wing's vascular structure. Repeating the procedure often produces varying locations of key wing features. Manual adjustment is often required to correct errors. Additionally, *WINGMACHINE* accepts only lower resolution  $480 \times 640$  pixel or  $240 \times 320$  pixel images, while the original images are  $1200 \times 1600$  pixels, losing a significant level of detail in the image resizing. Because of the measurement error and image resizing, much image data is discarded in order to calculate *low measurement error* shape and shape asymmetry measures of the wings [4].

A large number of shape measures to identify shape asymmetry have been reported in the literature, all based on the simple difference between paired wings of sums of distances between landmark points. For instance, the *Unscaled Directional Asymmetry (cent)* metric is the difference in *Centroid Size* between left and right wings, where *Centroid Size* is the square root of the sum of squared distances from the measured centroid to the set of low measurement area landmark points in the wing. Intuitively, the difference quantity can be a small number in magnitude and is thus potentially highly sensitive to measurement error in the creation of the shape measure for each wing. Errors in splining and image segmentation pose a potentially serious impediment to the scientific analyses.

This thesis discusses key features of the image data set and necessary background of image processing in Chapter 2. A range of segmentation methods are examined in Chapters 3 through 5, in order to find a more robust segmentation routine with which to calculate the current shape measures with lower measurement error and using a larger portion of the wing data. A summary comparison of the segmentation routines is made in Chapter 6, highlighting the

improved accuracy of the Frangi multi-scale method. Finally, in Chapter 7 the dimensionality of wing shape is explored through a principal components analysis of the wing image set, and alternate wing pair shape asymmetry measures developed from the covariance structure of the image set are proposed and compared to the existing asymmetry measures.

## CHAPTER 2

### IMAGE PROCESSING AND DATA SET DETAILS

#### Image Processing Basics

Figure 1 shows two equivalent computer representations of an image. The right representation is more immediately recognizable to the human eye as an image comprised of a foreground object and background. A more formal representation of a greyscale photograph as the image of a function over a 2d spatial domain is better represented visually by the left representation. In both visual representations, the  $m \times n$  image  $I$  is defined as:

$$I : [1, 2, \dots, m] \times [1, 2, \dots, n] \rightarrow \mathbb{R}$$

Theoretical continuity problems arise due to the discrete nature of the spatial domains. However, it is common (and necessary) to view the spatial domains as sampled points of  $\mathbb{R}^2$  in order to apply concepts and theory from disciplines such as vector calculus, differential geometry, and the like.

A common image preprocessing step is a *blurring* or a *sharpening* operation [5]. Blurring is typically accomplished via the convolution of the input image with some type of averaging filter, in effect smearing out overly fine detail and leaving larger image structures intact. In general, the larger the filter, the more blurring. In reality, the choice of filter type and size as well as filter parameters are tuned to the data sets at hand and thus is as much art as science. Blurring convolutions are employed throughout the methods as stipulated. A sharpening preprocessing step is also explored in the Maximal Gradient and Frangi methods of Chapters 4 and 5.

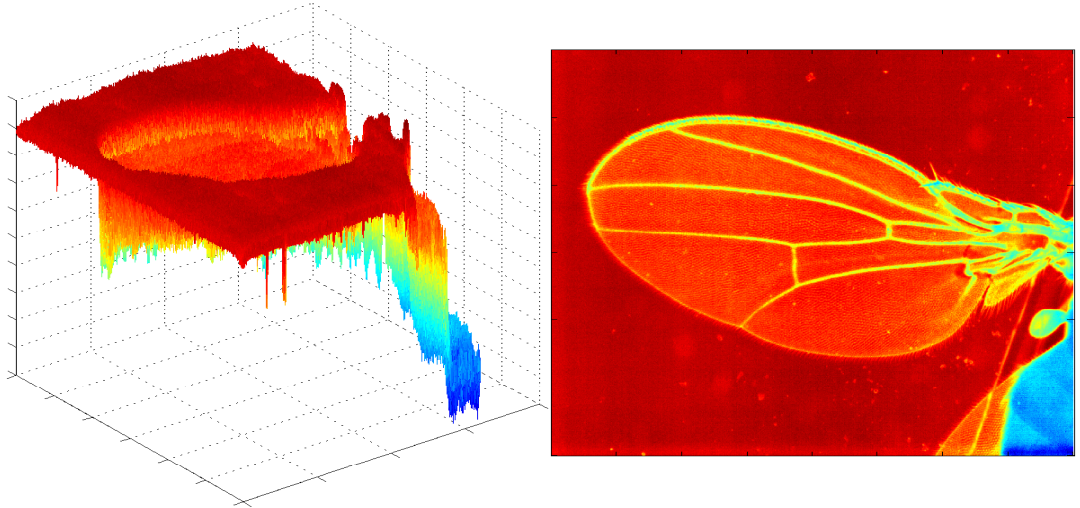


FIGURE 1: Computer image equivalents. (left) An image as the graph of a 2d function, and (right) an image as a 2d heat map of pixel intensity values.

### Image Data Set

#### Description

The image set analyzed herein is comprised of 48  $1200 \times 1600$  resolution grayscale images each containing a single *Drosophila* wing foreground and off-white background. The images were created and provided by the Carter Lab in the Biological Sciences Department of California State University, Long Beach. The benchmark asymmetry measures presented in this thesis were also provided by the Carter Lab, to serve as a representative sample of a class of asymmetry measures based on the measured distance between a set of landmark points on the fly wings. The image set and asymmetry calculations are available from the author or the Carter Lab upon request.

There are some variations *between* images in background intensity, and average pixel intensity, perhaps due to potential confounding factors such as ambient light differentials, power oscillations to the camera, position of photographer over the image object, grime in the fly wing capture device, or other confounding factors. In general, illumination variation in an image set is its own field of study though not pursued at length here, although a method to correct for it is implemented in the methods of Chapters 4 and 5.

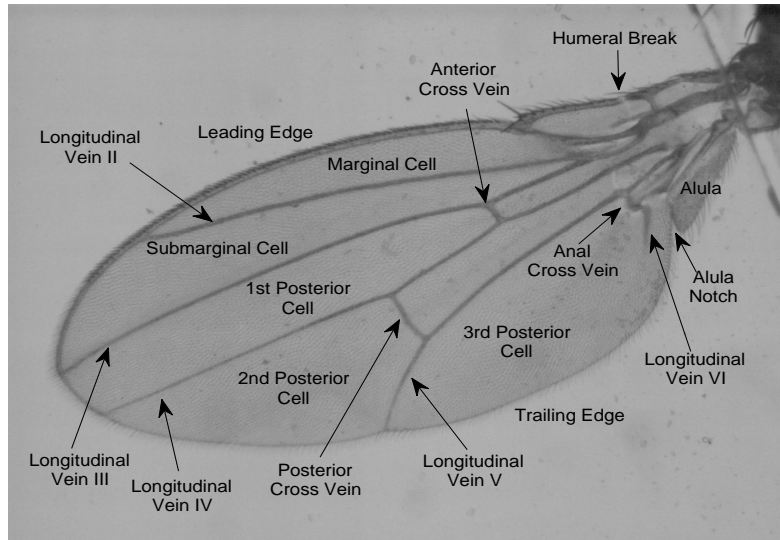


FIGURE 2: A representative wing image annotated with key features.

The wing images are characterized by left and right wings, determined by position of the fly body in the upper right or lower right corner of the image, respectively. Additional image objects include fly bodies and opposite wings. Extraneous image objects, including opposite wings on wing6BIG and wing26BIG and a partial occlusion of wing44BIG by its opposite wing, present a heterogeneity in the image set and a potential limiting factor in desired image segmentation outcomes.

Flywing anatomy nomenclature employed herein includes: (a) The thicker top horizontal external boundary, known as *the leading edge*, (b) the thinner bottom horizontal boundary known as *the trailing edge*, (c) the wing regions separated by horizontal (*longitudinal*) veins and the leading and trailing edges as *posterior, marginal* and *submarginal cells*, (d) the vertical veins separating the cells are the *posterior, anterior* and *anal crossveins*. An annotated representative wing image (wing45BIG) is provided in Figure 2, referencing all relevant wing features [6].

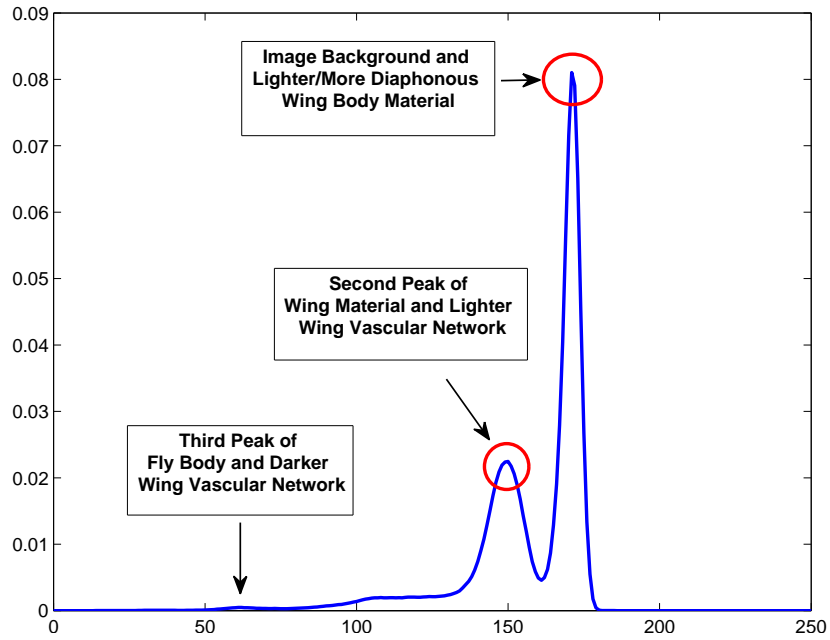


FIGURE 3: An image’s smoothed pixel intensity value probability distribution. Three separate modes are evident, each representing an image segmentation category and noise.

### Segmentation Potential

The raw unprocessed wing image is roughly divided into three modes of pixel intensity: (i) image background (higher intensity values), (ii) wing cell material and trailing edge (mid to high intensity values), and (iii) wing vascular structure, leading edge and fly body (lower intensity values). Figure 3 shows a representative smoothed probability distribution for wing45BIG. Overlap between the three modes of pixel distribution limit the potential of a purely thresholding based segmentation. For example, either lighter colored wing boundary will be included in the wing cell segmentation or darker colored wing cell will be included in the wing boundary segmentation. Inclusion of some wing cell material in the wing boundary segmentation is preferable, given the ability of further refinement of the segmentation via morphological operations to eliminate extraneous information.

The thinness and relative lightness of the trailing edge is problematic for any segmentation procedure, and suggests any blurring preprocessing will only

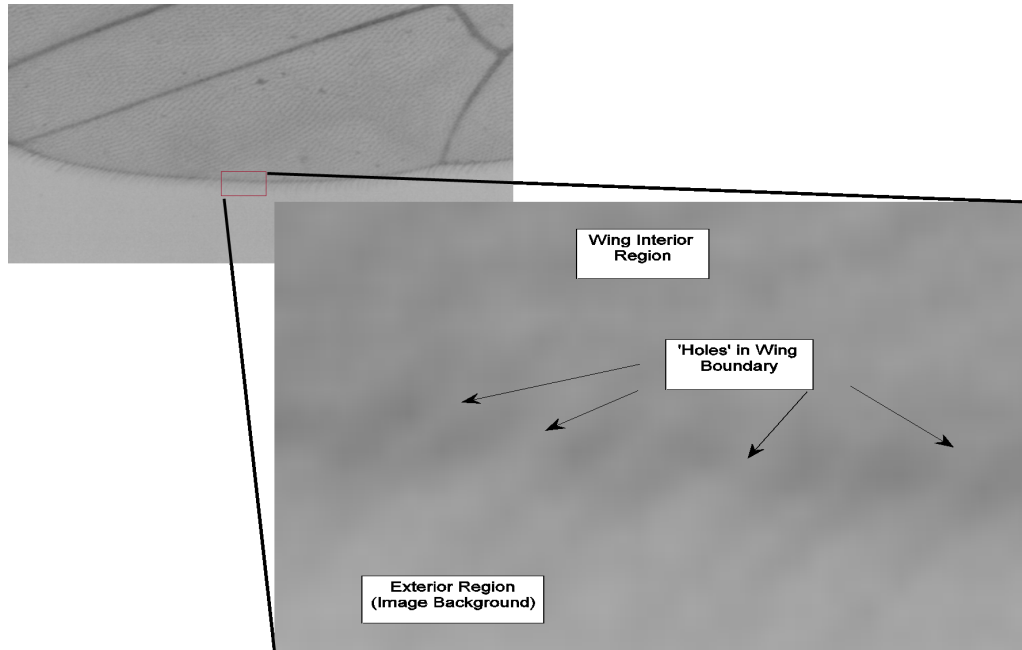


FIGURE 4: Issues in segmentation: close-up of wing45BIG trailing edge. A close-up zoom of a portion of the wing45BIG's trailing edge reveals it is not a continuous boundary separating the wing from the image background, posing an impediment to identification of the wing's exterior boundary as a closed curve.

exacerbate the difficulty in finding that portion of the wing boundary. Figure 4 shows a labeled zoom of a section of the trailing edge, where the discontinuity of the wing edge can be plainly seen.

A sharpening procedure is of merit and permits better segmentation results for the Maximal Gradient and Frangi methods. Sharpening procedures are unavailable for the adaptive histogram approach underlying the simple thresholding segmentation method, since the sharpening procedure eliminates the distinct mode of the image pixel distribution which represents the pixels interior to the wing cells. Applying a histogram based method on a sharpened image set would unavoidably produce massive oversegmentation of the veins, including large swathes of the wing cell pixels in the vein and boundary segmentation.

Partial differential equations-based variational methods must grapple with large image sizes. The Level Set method was implemented and its results are included in the segmentation summary, but the theory and implementation details are not discussed at length.

## CHAPTER 3

### ADAPTIVE THRESHOLDING METHOD

#### Overview

*WINGMACHINE* is a simple thresholding and morphological operations algorithm [7]. We create an intensity value thresholding algorithm as a suitable proxy baseline for *WINGMACHINE* to compare to the other segmentation methods developed herein. A thresholding-based segmentation method groups pixels based solely on their intensity value. For this data set, the distribution of image intensity values is trimodal. Each mode roughly corresponds to a segmentation region, though the distributions of pixel subpopulations – background, dark veins and fly body, and diaphanous wing cell pixels – overlap. As such, a simple thresholding method should not be expected to be the most accurate, since the natural consequence of the overlap of pixel subpopulations is necessary oversegmentation in the vein segmentation. Non-vein and boundary pixels need to be included in order to maximize the likelihood of inclusion of actual vein pixels in the vein segmentation. In this case, some wing cell pixels are unavoidably classified as vein pixels due to the overlap in intensity values. The core thresholding segmentation methodology is powerless to remedy this oversegmentation by its very nature.

Morphological operations therefore become necessary in order to (a) preserve and enhance the connectivity of the actual wing vein and boundary pixels and (b) eliminate the wing cell pixels in the vein segment which reduce the accuracy of the simple thresholding method. These goals are in conflict – in a simple discrete method like intensity value thresholding, there is no connectivity requirement of the vein pixels, nor is there a presumed closed boundary as in a variational segmentation method. In order to achieve the best possible

segmentation, wing cell pixels must be included in the vein segmentation, followed by postprocessing in order to redistribute misallocated wing cell pixels both physically close and intensity space close to vein pixels. This is achieved best through operations which do not connect previously unconnected image objects, preserving the integrity of the individual cells of the wing. Operations which also expand or shrink objects without regard to connectivity are also utilized as sparingly as possible, to, e.g., shrink away the cilia identified as wing boundary. Because of the difficulty in locating portions of the interior vascular network, distinct wing cells can be identified as a single connected component. These are a natural product of the segmentation method on this data set, and artificial creation of additional hybrid connected components from postprocessing is highly undesirable given their inherent mis-segmentation. Finally, applications of an area threshold are required to isolate the vein and wing boundary segmentation.

#### Adaptive Histogram Feature Analysis

Because of the variation between images in background lighting, differences in the intensity values across wings themselves, and other factors, we cannot use fixed intensity values to segment the images over the entire image data set. Therefore, we create an adaptive histogram approach, in which a smoothed probability distribution is fit to the frequencies of pixel intensity values using a non-parametric estimator of the distribution kernel (e.g., as opposed to stipulating a single-peaked normal distribution for each image). A smoothed distribution must be created because each individual sub-distribution corresponding to the image background, wing cell material or veins can itself be multi-peaked. The smoothest possible distribution is desired in order to find single modes which approximate a corresponding image segment that are *a priori* known to exist. An indexed array of probability densities at the 256 intensity values (since all raw images are class *wint8*, in which pixel intensity values may range across integers zero to 255) is then created. An approximation of the derivative of the probability density function is formed from simple differencing. The locations at which the derivative

approximation switches from positive to negative yield the local maxima image intensity locations of the probability density function. The two highest peaks correspond to the modes of image background pixels and wing cell pixels, as can be seen in Figure 3. Between these two peaks, the local minimum is also determined. It is postulated this local minimum is the best choice for the bifurcation point between the background pixel distribution and the wing cell pixel distribution.

### Algorithm Methodology

The trailing edge of the wing is of higher intensity values than a substantial number of pixels in the interior of the wing cells. Therefore, no segmentation method based solely on intensity values could possibly determine pixels in the wing's trailing edge to be members of the vein segmentation without inclusion of a substantial number of wing cell pixels in the segment. In order to minimize this potential oversegmentation, the task of determining the boundary of the wing with the image background is addressed separately from determining the wing's internal vein segmentation (as will be necessary in virtually all segmentation methods utilized).

### Finding the Leading and Trailing Edges

The background pixels to set to white by mapping image intensity values greater than the local minimum between the two peaks determined in the Adaptive Histogram algorithm to white. The image complement of the result yields the entire wing body plus cilia with some isolated blobs elsewhere. The largest image object is the isolated wing. The cilia is removed via a morphological erosion. Erosion is a technique to shrink image objects, which leaves only the set of foreground points in the image for which a structuring element centered at that point is itself entirely contained as a subset of the image foreground points. This operation leaves the leading and trailing edges of the wing with some error due to the asymmetry in cilia length both within a single wing image as well as across the data set. The erosion structuring element is manually determined through calibration to a sample image (wing30BIG). Because longitudinal vein V thins and

lightens considerably as it approaches the trailing edge (see Figure 2), the tail portion of it often fails to be included in the vein segmentation. In order to accomplish a segmentation which identifies the second and third posterior cells as distinct regions, the erosion structuring element size is set to shrink the wing perimeter in order to ensure intersection of the trailing edge with a segmentable region of vein V. This procedure enhances the connectivity of the vein segmentation (found immediately following in Subsection Finding the Interior Veins) with the exterior boundary segmentation, while introducing a repairable error in vein thickness (or, equivalently, an underestimate in the calculation of posterior and marginal cell areas is introduced in order to accurately identify the posterior and marginal cells as unique distinct areas).

#### Finding the Interior Veins

A conservative estimate of the boundaries of the vein segmentation in terms of pixel intensity values is required, so that maximal vein area is captured in the vein segmentation and not misidentified as wing cell. Masks from the image set's cut point data are created and applied to the output from the exterior boundary finder. Application of the mask can generate extraneous image objects from variations in fly placement, which are removed to yield the isolated wing. The isolated wing is then in turn itself used as a mask on the original image.

Pixels with intensities less than (the wing cell mode minus threshold parameter) are set to black. A parameter value of twelve was determined to be optimal, in a test range of ten to fifteen. This could also be further parametrised based on a value of the derivative of the probability density function, though given the low level of sophistication of the underlying segmentation method, better segmentation results are more likely the result of more sophisticated segmentation methodologies than the fine-tuning of parameters in the simple thresholding method. The vein segmentation is the resulting group of pixels with intensity values of zero.

The output is converted to a binary image with .01 threshold, and an area

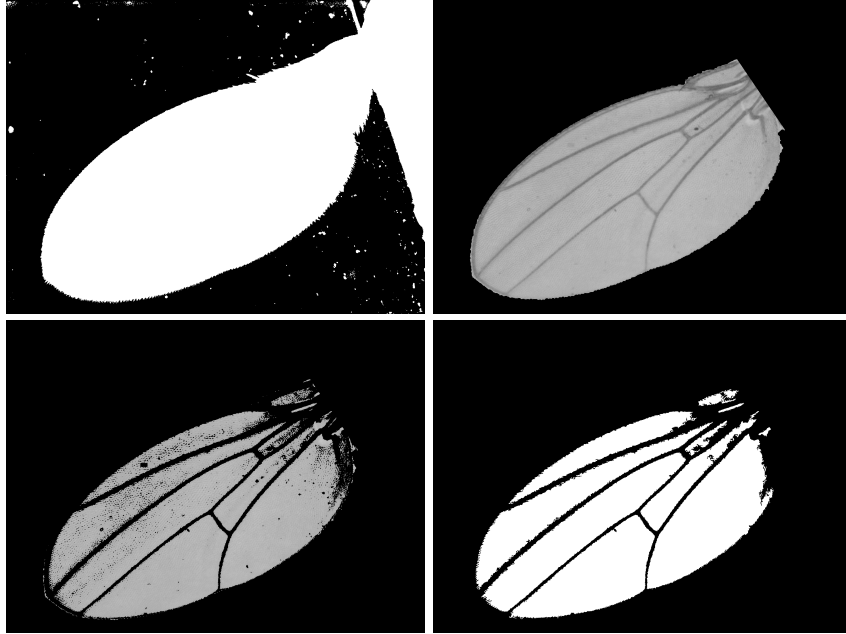


FIGURE 5: Adaptive Thresholding segmentation essential steps. (upper left) Locate the wing perimeter and area via a contrast stretch, (upper right) Isolate the wing interior with a wing area mask, (lower left) Locate interior vasculature, and (lower right) Repair wing cells from vein oversegmentation.

threshold of 500 pixels is applied. The image complement of the combination of the interior vein segmentation and the exterior boundary segmentation yields a complete segmentation of the wing. Figure 5 shows a subplot of the essential steps of the method.

## Results

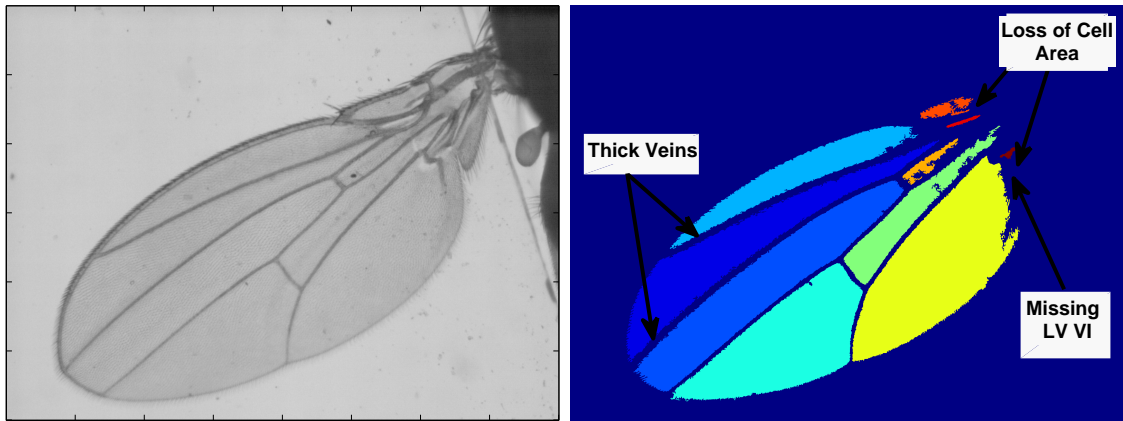


FIGURE 6: Example Adaptive Thresholding segmentation result (wing1BIG). In order to identify LV V through its intersection with the trailing edge, the vein segmentation needs to be oversegmented due to the lack of contrast with surrounding regions. The oversegmentation leads to thicker identified veins elsewhere, notable LV II and III. Darker pixel wing cell areas as well as small lighter pixel wing cell areas fail to be identified. LV VI fails to be identified as a result.

The necessary inclusion of darker wing cell material in the vein segmentation results in area loss in identified wing cells. Since this oversegmentation is not uniformly distributed, some unreparable distortion of area calculation and boundary location persists beyond the ability of morphological operations to redress. Less smooth cell boundaries result, as can be seen by the comparison between the raw wing image and the segmentation result in Figure 6.

Distinct colors represent isolated wing cells, which in turn indicates segmentation of that cell's boundary veins. As the longitudinal veins converge close to the wing's attachment to the fly body, wing cell pixel intensity values tend to be lower and are also included in the vein segmentation. The affected smaller wing cells then frequently fail any baseline area thresholding inclusion test. Thus the final wing segmentation fails to include these smaller cells. This area damage in the cells increases closer to the cut-line. The region of the third posterior cell to the right of the anal crossvein and longitudinal vein VI also fails to be identified.

## CHAPTER 4

### MAXIMAL GRADIENT SEGMENTATION

#### Gradient Segmentation Overview

Location of edges and boundaries between objects in images often corresponds strongly to the presence of a steep gradient in the image's intensity values, particularly where homogenous intensity value regions border other homogenous regions with different intensity values. Evaluation of the image gradient is a step in the direction of greater sophistication in image segmentation, through the calculation of an intermediate quantity with which to evaluate the image. Gradient-based methods have been shown to produce smoother and more accurate edge maps than thresholding methods [8].

#### Mathematics

In order to promote local or regional intensity value homogenization, an image is convolved with a Gaussian filter to smear out overly fine detail before other operations. A two-dimensional Gaussian kernel  $G(\mathbf{x}, \sigma)$  is given by:

$$G(\mathbf{x}, \sigma) = \frac{1}{2\pi\sigma^2} e^{-\frac{\|\mathbf{x}\|^2}{2\sigma^2}}, \quad \text{where } \mathbf{x} \in \mathbb{R}^2, \sigma \in \mathbb{R} \quad (4.1)$$

and where  $\|\cdot\|$  denotes the standard  $\ell^2$  norm. The smoothing effect of the kernel on a wing boundary region is shown in Figure 7.

Although the true domain of an image  $I$  is a finite subset of  $\mathbb{N}^2$ , in order to draw on necessary notions like continuity, the image domain is implicitly thought of as  $\mathbb{R}^2$  when invoking theory and abstract concepts, and  $\mathbb{N}^2$  is explicitly invoked when presenting actual calculations on the discrete pixel grid. Considering image  $I$ 's spatial domain as  $\mathbb{R}^2$ ,  $I(\mathbf{x}) = I(x, y)$ , spatial differentiation of  $I$  after

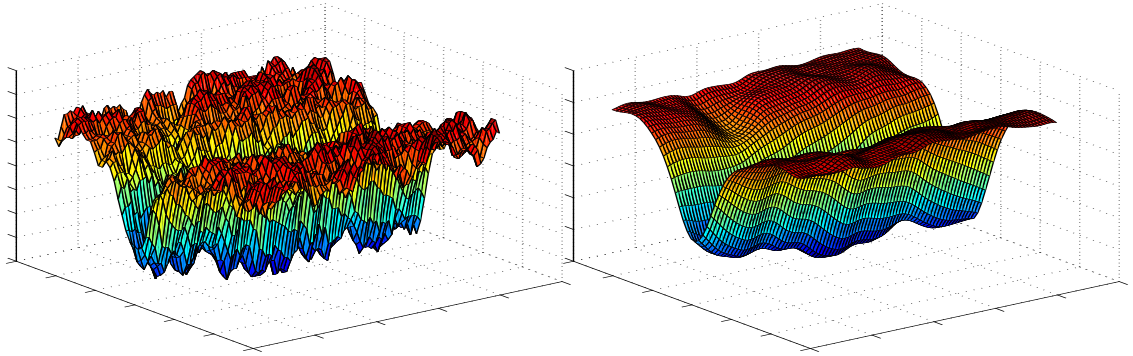


FIGURE 7: Wing boundary region before and after smoothing.

convolution with  $G$  exhibits the particularly useful property:

$$\frac{\partial}{\partial x} [G(\mathbf{x}, \sigma) * I] = \left[ \frac{\partial G(\mathbf{x}, \sigma)}{\partial x} \right] * I \quad (4.2)$$

Also, since

$$\frac{1}{\sqrt{2\pi\sigma^2}} e^{-\frac{(x^2+y^2)}{2\sigma^2}} = \frac{1}{\sqrt{2\pi\sigma^2}} e^{-\frac{x^2}{2\sigma^2}} \times \frac{1}{\sqrt{2\pi\sigma^2}} e^{-\frac{y^2}{2\sigma^2}}$$

it follows directly that convolution with a 2d Gaussian kernel is equivalent to iterated convolutions with 1d kernels.

Therefore, each gradient component is calculated as the 1d convolution of the image with the derivative of the Gaussian kernel. In the horizontal dimension, this means passing the 1d Gaussian derivative kernel over each row of the image, padding each side of the image with ghost cells to accommodate the length of the kernel at the boundary of the image. Since the length of the 1d kernel for standard choices of  $\sigma$  is significantly smaller than either the length or width of the image, fewer computations are necessary to calculate a gradient field.

The derivative approximation in each spatial dimension is performed as a centered differences calculation except at the boundary points of the kernel, where forward differences are utilized. Invoking the finite subset of  $\mathbb{N}^2$  domain, the actual centered difference partial derivative of image  $I$  with respect to the horizontal

dimension (' $x$ ') at point  $(i, j)$ , where  $i$  is the row index and  $j$  is the column index, is given by:

$$I_x(i, j) = \frac{I(i, j + l) - I(i, j - 1)}{2} \quad (4.3)$$

### Strong and Weak Edges

Even smoothed images still exhibit some noise, for a standard range of  $\sigma$ . It is more likely than not in most data sets that no  $\sigma$  exists for which the convolution with the kernel will retain all relevant image structure and remove all extraneous detail. Since the gradient is a vector field defined on the entire image domain, an evaluation of the relative magnitude of a pixel's gradient value is necessary in order to classify the pixel as a member of an object boundary. Not all pixels with non-zero gradient magnitudes are boundary locations, as can be seen in the gradient quiver plot over a vessel boundary in Figure 8. In order to better classify pixels, a threshold level of gradient magnitude for boundary pixels must be determined. This can be accomplished through either (a) an *a priori* assumption of the number of pixels in the image which are boundary pixels and finding the corresponding gradient magnitude from the gradient magnitude's cumulative frequency histogram, or (b) specification of a threshold level of gradient magnitude for boundary classification. The pixels which possess a larger magnitude gradient than the threshold are then classified as boundary pixels.

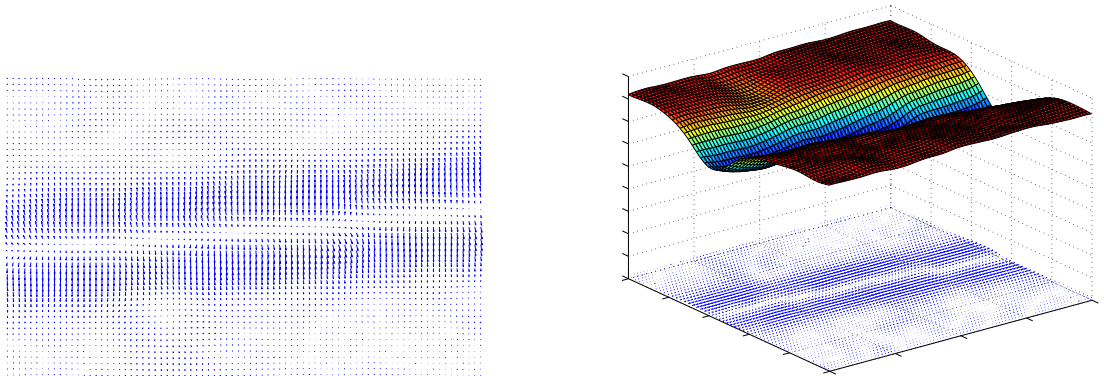


FIGURE 8: Gradient quiver plot of a vein region. (left) Gradient quiver plot of a vein region and (right) under a vein region graph.

In order to better retain image structure and remove spurious noise, the gradient magnitude schematic is further refined by defining threshold values for both *strong* and *weak* edges, where a weak edge pixel is a pixel for whom (a) the gradient magnitude is above some lower-than-strong threshold level and (b) the pixel is bordering a pixel classified as a strong edge. The strong edge classification can then be set at a larger gradient magnitude level, eliminating much image noise, while the retention of the second-tier weak edge captures boundary pixels with lower gradient magnitudes. This dynamic can be seen in longitudinal vein V as it thins and lightens as it approaches the trailing edge. Because the gradient magnitudes at the vein boundary are relatively low, setting the strong edge threshold low enough to include these pixels in the strong edge segmentation will necessarily retain much spurious segmentation, while the two-tiered approach circumvents this problem.

In order to determine the presence of weak and strong edges, the gradient components are calculated via convolutions of the image with 1d Gaussian derivative kernels. The approximate angle the gradient vector forms to the vector  $(1, 0)$  is determined by evaluation of sign of each of the spatial partial derivatives and a comparison of the magnitude of both gradient components,  $I_y$  and  $I_x$ . The angle is assigned to a direction as determined by  $45^\circ$  increments. For instance, where both spatial partial derivatives of the image are positive, and  $I_y > I_x$ , the gradient vector forms an angle of between  $45^\circ$  and  $90^\circ$  with the vector  $(1, 0)$ . More exact calculation of the gradient angle is not productive, due to the discrete nature of the domain.

For each  $45^\circ$  direction, arrays the same size as the underlying image are formed in which the only non-zero values are the gradient magnitudes of pixels with gradients pointing in that direction. In this array, the gradient magnitude of each pixel is then compared with the gradient magnitudes of the pixels neighboring it in the direction given by the gradient (both forwards and backwards neighbors, allowing only four directions to be evaluated). Pixels which have a local

maximum in gradient magnitude are classified as *Local Max* pixels. Iterated over each direction, a total Local Max pixel map covering the entire image domain is formed. Application of the strong edge threshold isolates pixels to be classified as strong edges, and application of the weak edge threshold and strong edge connectivity test yield the weak edge. The combination of strong edge pixels and weak edge pixels form the identified object boundary. Since image gradient fields exhibit spatial coherency, the Local Max approach is effective at identifying image boundary locations.

To demonstrate the sensitivity of the method to the parametrisation of weak and strong edges, as well as the scale to the Gaussian filter, a default implementation ( $\sigma = \sqrt{2}$  and unspecified weak and strong edge threshold values) is run on both raw and sharpened wing3BIG images. As seen in Figure 9, the routine returns a drastic oversegmentation. A default implementation is unsuccessful at identifying image structure of interest, because of the assumption that must be made about what magnitude of gradient constitutes a strong edge in the input image. The default assumption is that 70 percent of pixels in the image are not edges, and thus sets the strong edge threshold at the 70th percentile of pixel gradient magnitudes. Because of the abundant striations in the wing, the strong edge threshold is set too low and the algorithm is unable to isolate boundaries of interest from what the human eye perceives to be relatively homogenous regions.

#### Algorithm

Sharpened images (see section Sharpening Preprocessing for details of the sharpening procedure) are segmented immediately. Parameter calibration yields maximally useful ranges of values for the data set of 0.0001 – 0.03 for the low threshold and 0.25 – 0.30 for the high threshold, with  $\sigma$  of three and four, respectively. As the left image in Figure 10 shows, the strong gradient segmentation engine yields delicate single pixel thick boundaries. A zoom of this image on the right reveals some of the impediments to accurate segmentation of desired features only. Some cilia are included in the segmentation, and some



FIGURE 9: Abundance of image gradient in wing images. The image gradient retention threshold in a default implementation of the Maximal Gradient segmentation algorithm drastically oversegments the image. Striations in interior wing cells are identified as boundary pixels, preventing isolation of the true wing boundaries. Because of the abundance of image gradient in the image, the method is sensitive to the parametrisation of gradient magnitude level for edge classification.

portions of the interior wall of the veins and wing boundary are only partially identified. These lines often abruptly end, forming open regions which leave the routine prone to connecting interior cells as single regions as well as identifying portions of the vascular structure as wing cells. In order to counter this tendency, the raw segmentation is thickened and dilated to enhance connectivity. After application of the cutpoint mask, an attempt to separate lightly connected components is made through erosion of segmentation objects. Area loss from the erosion is corrected through a thickening of the resulting segmentation objects, which does not enhance connectivity. A ‘poor-man’s inpainting’ method was explored, which sought to connect the skeleton endpoints (a segmentation line that ends in a point and does not form a closed region) to the closest point on the remaining segmentation by evaluating lengths of lines from the point to intersection at 45 degree intervals. The routine slowed the segmentation

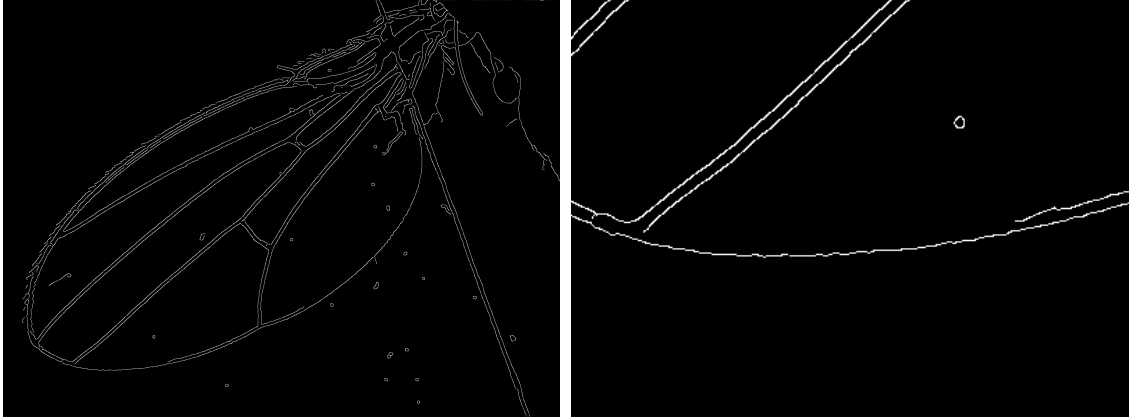


FIGURE 10: Raw Maximal Gradient output on wing3BIG. (left) The calibrated segmentation routine isolates the wing vasculature and exterior boundary as edges. (right) A zoom of the second posterior cell near the wing tip shows that some of the identified boundaries are discontinuous, requiring postprocessing to identify the wing cells as distinct areas. Also evident is separate identification of both the interior and exterior boundary of each vein.

considerably while not materially improving the result over the cycle of enhancing and destroying connectivity in the core method.

### Result

Since the leading edge is thick and long, the algorithm is prone to identify portions of it as distinct regions of interest, instead of as a boundary separating the image background from the marginal and submarginal cells. The erroneous regions can survive area thresholding of connected components to remove extraneous data due to its size. In order to correct for this, morphological operations which enhance connectivity of unconnected components are applied and force absorption of the leading edge regions into the marginal and submarginal cells. Asymmetric area error is then introduced due to the inherently universal application of the morphological operation with only a need where the erroneous areas exist. An alternative would be to allow the erroneous regions to survive and exist as part of the final segmentation, which itself then would preserve error. In Figure 10 both results can be seen – the orange segment near the humeral break is a surviving region of the leading edge, while the exterior boundary of the second and third posterior cells exhibit absorption of portions of the trailing edge.

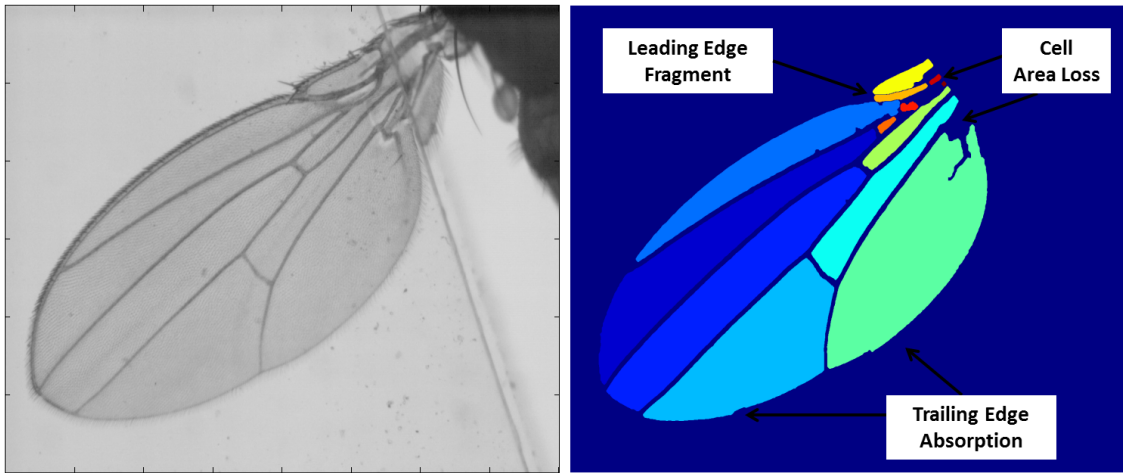


FIGURE 11: Example Maximal Gradient segmentation result (wing3BIG). (left) Wing3BIG image, and (right) the segmentation result. The vascular network is well identified, although the light orange segment is an erroneous identification of a portion of the leading edge as a wing cell area. The second and third posterior cells exhibit erroneous absorption of portions of the trailing edge.

Although not as problematic as in the Adaptive Thresholding segmentation, small regions near the cut line are prone to be unsegmented, because of a lack of strong edges (non-maximal gradients due to greater intensity homogeneity) as well as non-closed boundary edge detection.

## CHAPTER 5

### FRANGI MULTI-SCALE SEGMENTATION

#### Scale Space

An image is a “physical observable with an inner and outer scale bound” [9]. The inner scale bound of an image is a single pixel, in that any additional information available in the photographed scene at sub-pixel size is lost upon the acquisition of the image. The outer scale bound is the image frame – obviously an object larger than the image frame is not able to be completely captured in the image. However, in between these inner and outer scale bounds necessarily will be image objects of potentially varying scales. For instance, a photograph of a tree will include the tree itself as a single large object, although at smaller scales may also be the shapes and locations of individual leaves as objects (or patterns in bark, or a butterfly flying near the tree, etc.). The image itself can then be viewed as a union of these varyingly scaled objects. A key insight in multi-scale segmentation is that objects in these individual *scale spaces* are separable.

In fact, the very nature of the image acquisition makes a scale-space representation intrinsic and unavoidable. Because information is lost by the lower bound of image resolution, any given image must be viewed as a convolution of the true physical observable  $I_0$  with a filter of unknown size  $\hat{\sigma}$ .  $\hat{\sigma}$  must be unknown, since the amount of detail lost in the imaging is unknown. Necessary scale-space constraints like symmetry, linearity and avoidance of creation of spurious detail dictate the filter must be in the family of Gaussian kernels [9]. Therefore, any 2d image  $I(\mathbf{x}) = I(x, y)$  can be represented as:

$$I(\mathbf{x}) = I(\mathbf{x}, \hat{\sigma}) = G(\mathbf{x}, \hat{\sigma}) * I_0$$

where  $G(\mathbf{x}, \sigma)$  is the Gaussian filter introduced in Chapter 4.

## Multi-Scale Segmentation

Multi-scale segmentation is a natural evolution from lower-level gradient-based edge detector segmentations such as the Maximal Gradient method of Chapter 4. The image gradient is still recognized as the most relevant information to find boundaries and segment images. However, lower-level gradient based methods often fail because they implicitly assume only one spatial scale of interest exists. Often times, the spatial scale of interest is the pixel scale by default, and the user must apply any other scale as a preprocessing step. In the pixel scale case, only very local changes in image intensity can possibly be registered using any standard gradient stencil. The lowest-level gradient methods then pick up sharp edges, but fail at edges of larger scale and softer edges like shadows. The Maximal Gradient method does implicitly recognize that the scale of image objects may not be at the local pixel level by embedding a single convolution with a Gaussian kernel of parametrised width  $\sigma$ . Still, though, the scale space is essentially fixed by the parametrised kernel width. Because images may have structures at multiple scales, the Frangi method and the entire family of multi-scale methods establish a more robust method for boundary detection by iteratively evaluating the image gradient at multiple scales. The Frangi method has been shown to segment vessels in noisy medical image sets with high accuracy [10].

Interestingly, the foundational underpinnings of the multi-scale approach are found in biological vision systems. The study of Receptive Field profiles such as vision suggests they are best modeled by Gaussian filters and their partial derivatives [9]. In practice, multi-scale methods iteratively evaluate the image gradient by convolving the image with the partial derivatives of a Gaussian filter of multiple widths (*i.e.*, for a range of  $\sigma$  values). The method establishes a likeliness measure a pixel is an edge from the set of the pixel's gradient values at each scale. The likeliness measure at each scale is formed via an analysis of the curvature of the image surface evaluated at each pixel.

## Mathematics

### Curvature: One Spatial Dimension

Recall that the approximation of a function of a single variable at a point  $x_0 + \Delta x$  is given by:

$$f(x_0 + \Delta x) \approx f(x_0) + \Delta x f'(x_0) + \frac{1}{2} \Delta x^2 f''(x_0)$$

Consider the example  $f(x) = x^2$ . Given the value of  $f$  at  $x = 1$ , the first degree approximation for  $f$  at  $x = 2$  is  $f(1) + f'(1) = 3$ . Employing only the linear correction term of  $f'(1)$  yields an error of one. The first degree approximation neglects the curvature of the estimated function. The second-order term of the Taylor expansion recovers (much of) the curvature in the estimation by providing the approximation a quadratic term.

### Curvature: Two Spatial Dimensions

Exactly analogous to the 1d case, the second-order Taylor expansion approximation of a function of two variables  $f$  at point  $(x_0 + \Delta x, y_0 + \Delta y)$  yields the local properties of the surface near the point:

$$\begin{aligned} f(x_0 + \Delta x, y_0 + \Delta y) \approx & f(x_0, y_0) + \Delta x \cdot \frac{\partial f}{\partial x}(x_0, y_0) + \Delta y \cdot \frac{\partial f}{\partial y}(x_0, y_0) \\ & + \frac{1}{2} \left[ \Delta x^2 \frac{\partial^2 f}{\partial x^2}(x_0, y_0) + 2\Delta x \Delta y \frac{\partial^2 f}{\partial x \partial y}(x_0, y_0) + \Delta y^2 \frac{\partial^2 f}{\partial y^2}(x_0, y_0) \right] \end{aligned}$$

Since an image domain is 2d, this Taylor expansion can be applied directly to an image domain. An image  $I$  is thus locally approximated near point  $\mathbf{x}_0 = (x_0, y_0)$  by:

$$I(\mathbf{x}_0 + \Delta \mathbf{x}) \approx I(\mathbf{x}_0) + \Delta \mathbf{x} \nabla I(\mathbf{x}_0) + \Delta \mathbf{x}^T \mathcal{H} \Delta \mathbf{x} \quad (5.1)$$

where  $\mathcal{H}$  is the *Hessian* matrix of  $I$ :

$$\mathcal{H} = \begin{bmatrix} I_{xx} & I_{xy} \\ I_{xy} & I_{yy} \end{bmatrix}$$

As in the 1d case, the curvature of the surface at a given point is measured by how far the surface deviates from its tangent plane. However, curvature of a surface over two spatial dimensions is a more complicated mathematical quantity, because there are infinite directions in which to evaluate the quantity. Analogous to the 1d case, the curvature of the surface can be approximated by the second-order term of the Taylor approximation.

### Ordering the 1d Curvatures Embedded in a 2d Surface: The Principal Curvatures

By definition, the *principal curvatures* at a point on a surface are the maximum and minimum values of the *normal curvature* of all curves on the surface that pass through the point. As shown visually in Figure 12, for a curve  $\gamma(s)$  on a surface  $\Phi$ , where  $s$  is the arc length parameter, the normal curvature  $k_n$  of the curve at the point is the magnitude of the projection of  $\ddot{\gamma}$ , the second derivative of the curve with respect to the arc-length parameter, onto the principal unit normal vector  $N$  of the surface [11].

The principal vectors are tangent to the curves of maximum and minimum normal curvature. Therefore, the principal curvatures of a surface yield the directions of most and least change of the surface from its tangent plane. Since edges and boundaries in images are associated with large curvature in the surface formed by the graph of the image function, the principal curvatures yield the most likely direction of an edge and most likely direction of image object continuity, from the maximum and minimum principal curvature values, respectively.

The principal curvatures are the roots of  $\det(\mathcal{F}_{II} - k\mathcal{F}_I) = 0$ , where  $\mathcal{F}_{II}$  is the *second fundamental form* of the surface, which for surfaces that are graphs of functions of two variables (like the image function) is equivalent to the Hessian

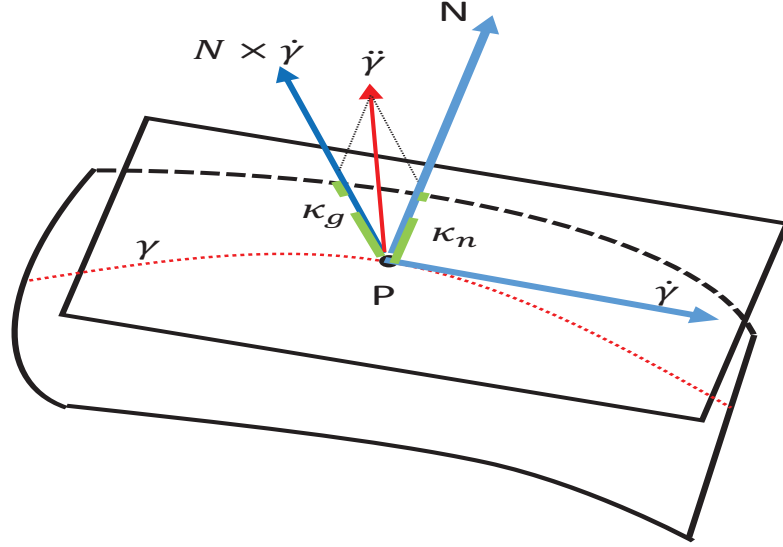


FIGURE 12: Normal curvature of a space curve. At any point, the normal curvature  $k_n$  of a curve  $\gamma$ , parametrised by arc length, is the magnitude of the projection of  $\ddot{\gamma}$  onto the principal normal vector to the surface.

matrix,  $k$  are the principal curvatures and  $\mathcal{F}_{\mathcal{I}}$  is given by the *first fundamental form* for the surface, which is a measure of the length of curves on the surface [11].

For a curve  $\gamma$  parametrised by time  $t$ , its arc length  $s$  is

$$s = \int_{t_0}^t \|\dot{\gamma}(z)\| dz$$

where  $\dot{\gamma}$  is the first derivative of the curve with respect to time. For a curve on the surface,  $\gamma(t) = \Phi(x(t), y(t))$ , and then  $\|\dot{\gamma}(t)\|^2 dt$  gives the first fundamental form

$\mathcal{F}_{\mathcal{I}}$ :

$$Edx^2 + 2Fdx dy + Gdy^2 = d\mathbf{x}^T \mathcal{F}_{\mathcal{I}} d\mathbf{x}$$

$$\mathcal{F}_{\mathcal{I}} = \begin{bmatrix} E & F \\ F & G \end{bmatrix} = \begin{bmatrix} \Phi_x^2 & \Phi_x \cdot \Phi_y \\ \Phi_x \cdot \Phi_y & \Phi_y^2 \end{bmatrix}$$

For the image surface,  $\mathcal{F}_{\mathcal{I}}$  is given by

$$\mathcal{F}_{\mathcal{I}} = \begin{bmatrix} 1 + I_x^2 & I_x \cdot I_y \\ I_x \cdot I_y & 1 + I_y^2 \end{bmatrix} \quad (5.2)$$

However, Frangi approximates the principal curvatures of the surface by implicitly assuming the image surface is locally isomorphic to a plane at a given point. This reduces  $\mathcal{F}_{\mathcal{I}}$  to the identity matrix. In the Frangi approximation, the principal curvatures of the surface are the eigenvalues of the Hessian matrix  $\mathcal{H}$  evaluated at the point:

$$\det \begin{bmatrix} I_{xx} - k & I_{xy} \\ I_{xy} & I_{yy} - k \end{bmatrix} = 0 \quad (5.3)$$

Since  $\mathcal{H}$  is real and symmetric, the eigenvalues are known to be real. Also, eigenvectors of distinct eigenvalues are orthogonal, therefore the principal curvatures and their associated principal vectors extract two orthonormal directions of most and least curvature and the amount of curvature in each direction is the magnitude of the eigenvalue.

#### Sharpening Preprocessing

Due to the low contrast between striations in the wing cells near the vascular structure and some portions of the vascular structure, a sharpening preprocessing step is of merit. This *tophat* procedure subtracts an estimate of the image background from the image and is known to enhance contrast and can correct for any non-uniform illumination, in which like objects have different pixel intensity values due to physical location in the image frame [5]. A related *bottomhat* procedure further enhances contrast in the image [5]. Figure 13 shows wing15BIG after sharpening. The sharpening creates more pronounced striation in the wing cells, which has the desired effect of slightly shifting darker pixels in the cells away from the vascular network and exterior edges. This allows for higher accuracy in locating the actual vein edges, as seen in a side by side comparison of the raw output of the Frangi edge detector with and without sharpening in Figure 14.

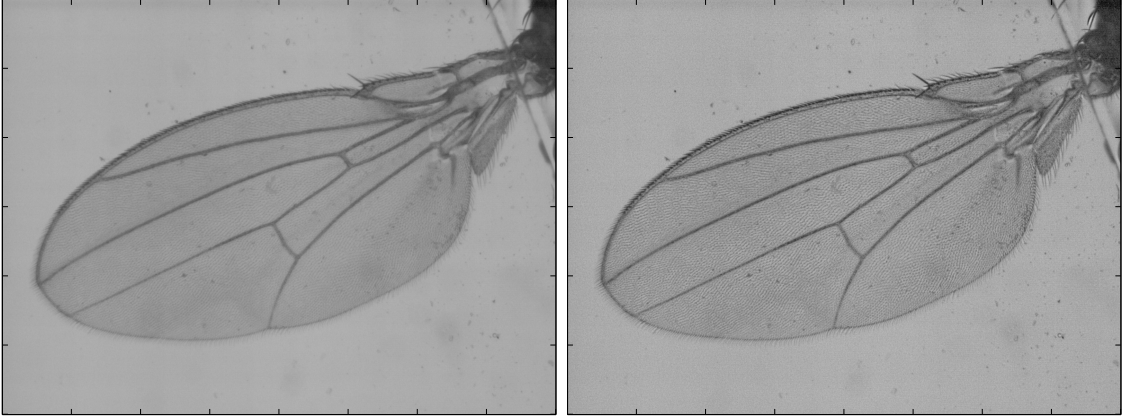


FIGURE 13: A comparison of the original and sharpened image. (a) Original wing45BIG (b) Sharpened image

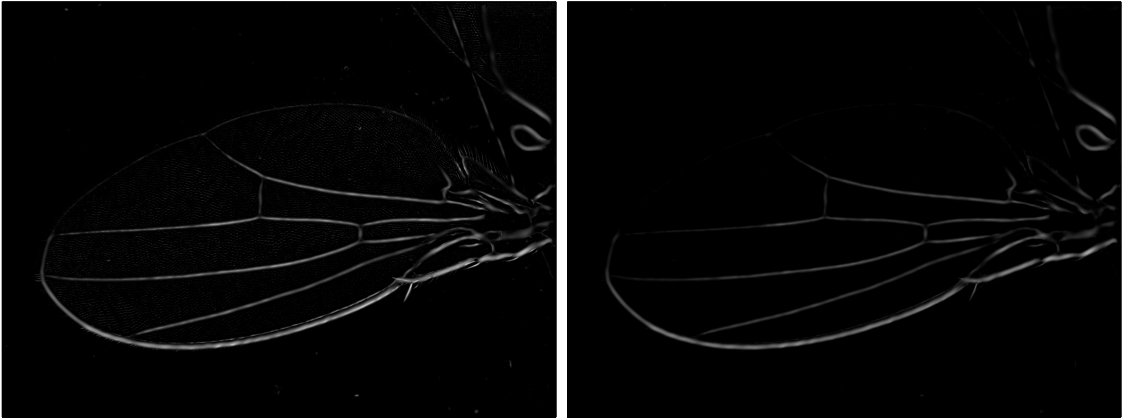


FIGURE 14: Raw output of the Frangi edge detector. (left) With a sharpening pre-processing step and (right) without sharpening. The sharpening procedure creates greater pixel-scale gradient, which the Frangi detector is able to detect, as evidenced by the better identification of the entire vein segmentation.

### Frangi Segmentation

In a multi-scale method, the scale space is parametrised with scale parameter  $s$ , where  $s$  is the width of the Gaussian filter:

$$I(\mathbf{x}_0 + \Delta\mathbf{x}, s) \approx I(\mathbf{x}_0, s) + \Delta\mathbf{x}\nabla I(\mathbf{x}_0, s) + \Delta\mathbf{x}^T \mathcal{H}(\mathbf{x}_0, s) \Delta\mathbf{x} \quad (5.4)$$

At each scale, the directions of most and least change in curvature of the convolved image surface are computed. Frangi et al. [12] postulates that if the principal curvatures are roughly equal in magnitude,  $|k_1| \approx |k_2|$  where  $k_1$  and  $k_2$  have been ordered such that  $|k_1| \leq |k_2|$ , then the pixel is more likely a member of a

‘blob-like’ structure, since there is no preferred direction for change in image surface level. However, when  $|k_1| \ll |k_2|$ , and  $|k_1| \approx 0$ , the pixel is more likely to be a vein pixel, since veins and external boundaries are characterized by long length and thin width (‘tubular’). Thus, the eigenvalue decomposition provides an elegant metric for evaluation of ‘vesselness’ at any given scale.

At each scale, as represented in Table 1, a pixel is more likely to be a vein according to the following heuristic principles (where L is low magnitude, H is high magnitude and  $\pm$  is sign of the eigenvalue): (a) Where  $k_1$  and  $k_2$  have been ordered such that  $|k_1| \leq |k_2|$ , one eigenvalue must be much larger than the other in magnitude in order to select for tubular structures. (b) Only one of the eigenvalues should be close to or identically zero. If both eigenvalues are near zero but still form a large ratio (e.g.  $k_1 = .001$ ,  $k_2 = .01$ ) then the pixel is most likely to be a background pixel.

TABLE 1: Frangi 2d Pixel Classification Heuristic

Frangi Vesselness Heuristic		
$k_1$	$k_2$	Structure Pattern
L	L	no direction
L	H-	bright tubular
L	H+	dark tubular
H-	H-	bright blob
H+	H+	dark blob

Note: The magnitude and sign of the Hessian matrix’s eigenvalues determine the local geometry of the image surface and the consequent classification of the pixel as a vein pixel, blob pixel, or other.

For dark vasculature as in the image set, Frangi captures the heuristic principles for vesselness at each scale in the metric  $\mathcal{V}_0(s)$ :

$$\mathcal{V}_0(s) = \begin{cases} 0 & \text{if } k_2 < 0 \\ e^{-\frac{\mathcal{R}_B^2}{2B^2}}(1 - e^{-\frac{s^2}{2c^2}}) & \text{if } k_2 \geq 0 \end{cases} \quad (5.5)$$

where  $\mathcal{R}_B = k_1/k_2$  is the eigenvalue proportionality measure reflecting principle (a)

above, and

$$\mathcal{S} = \|\mathcal{H}\|_{\mathcal{F}} = \sqrt{k_1^2 + k_2^2}$$

is the Frobenius matrix norm used to select for presence of structure representing principle (b) above.  $\mathcal{B}$  and  $c$  are parameters to control the sensitivity of the method to  $\mathcal{R}_{\mathcal{B}}$  and  $\mathcal{S}$ , respectively. Because the principal curvatures have been labeled such that  $|k_1| \leq |k_2|$ ,  $|\mathcal{R}_{\mathcal{B}}| \leq 1$ . When  $|\mathcal{R}_{\mathcal{B}}|$  is near 1, the principle curvatures are close in magnitude, making the pixel likely to be a blob, and thus the vesselness measure is made smaller. The final vesselness measure  $\mathcal{V}_F$  for each pixel is simply the largest vesselness measure over the range of scales at which the method is evaluated:

$$\mathcal{V}_F = \max_{s_{min} \leq s \leq s_{max}} \mathcal{V}_0(s) \quad (5.6)$$

The vesselness measure of the sharpened wing images is determined over scales one, three, five, seven and nine with optimal parameter values  $c = 800$  and  $\mathcal{B} = 0.845$  in the core Frangi engine. Although Frangi et al. suggest the Frangi method returns an intermediate result to be fed into another edge detector, better results here are achieved by working directly with the Frangi output. The Frangi vesselness measure is converted to a binary image with a binary threshold of 0.01 (on a scale of zero to one) – in effect all structure identified as possibly a vessel is retained. After application of an area thresholding of 500 pixels to isolate connected objects of interest, light connectivity enhancements are applied to repair undersegmentation from missing vein segment patches. Still the trailing edge and the thin end of longitudinal vein V are not continuously selected as edges. As such, the segmentation of the wing’s exterior boundary must again proceed separately from the interior vascular network. The exterior boundary is found as described in Section Finding the Leading and Trailing Edges.

Separation of the wing from the fly body is again performed as in Section Adaptive Thresholding Results. Although less wing cell area is erroneously identified in the vein and boundary segmentation in the Frangi segmentation

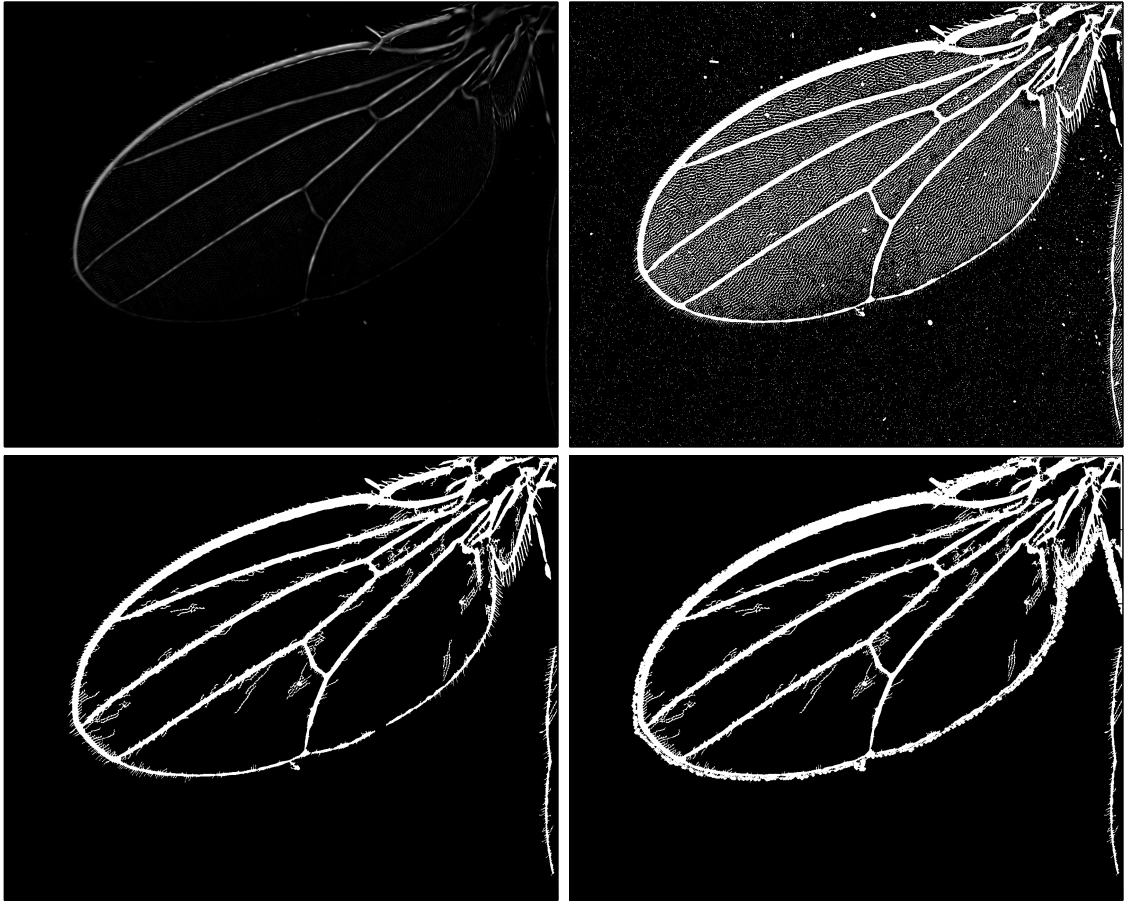


FIGURE 15: Frangi segmentation essential steps. (upper left) Frangi edge detector output, (upper right) Convert raw output to a binary image with .01 threshold, (lower left) Area thresholding to remove extraneous data and make light connectivity enhancements to bridge small pixel gaps in vascular network, and (lower right) Addition of the exterior boundary found in Chapter 3.

method than in previous methods, the close physical proximity of wing cell striations to the vasculature network does lead to inclusion of striation filaments in the vein segmentation. As such, morphological operations to repair the area loss of segmented cells due to the unavoidable inclusion of darker wing cell pixels in the vein segmentation is done, as described previously in Sections Overview, Finding the Leading and Trailing Edges, and Adaptive Thresholding Results, respectively.

### Results

The Frangi method achieves a higher degree of segmentation accuracy, as shown in Table 2 in Chapter 6. Most of the internal wing vasculature is identified with a minimum of erroneous inclusion of darker cell pixels, due to the

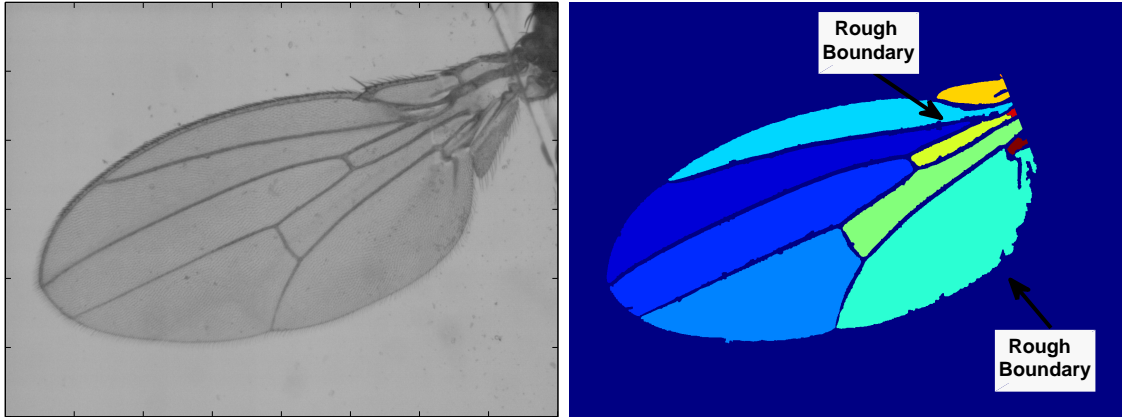


FIGURE 16: Example Frangi segmentation result (wing45BIG). (left) Original image, and (right) The segmentation result. The vascular network is well identified, including longitudinal vein VI. Small wing cell areas near the cut line are preserved. The third posterior cell boundary is rough, due to the inclusion of striation filaments in the trailing edge segmentation.

combination of the Frangi method itself with the particular sharpening preprocessing step. The core Frangi filter frequently fails at finding longitudinal vein V where it thins as it approaches the trailing edge as well as the previously discussed failure to find the trailing edge, necessitating *a*) a separate treatment of the trailing edge segmentation as discussed in Section Finding the Leading and Trailing Edges, and *b*) postprocessing morphological operations to enhance the connectivity of the interior vascular network previously discussed. In an improvement over the Maximal Gradient method, Frangi does not identify separate boundaries for the interior and exterior edges of the leading edge. Smaller areas near and beyond the cut-line are also correctly identified as wing cells. The full segmentation is shown in Figure 16. In a significant improvement over previous methods, longitudinal vein VI is accurately segmented and the third posterior cell area to the right of the vein is included in the segmentation. The location of the leading edge is identified with high accuracy, as can be seen in a side by side zoom of the segmentation result and the original image in Figure 17. The difficult longitudinal vein V is also accurately identified, as shown in a side by side zoom of the segmentation result and the original image in Figure 18. Local error in placement of the trailing edge along the bottom of the third posterior cell

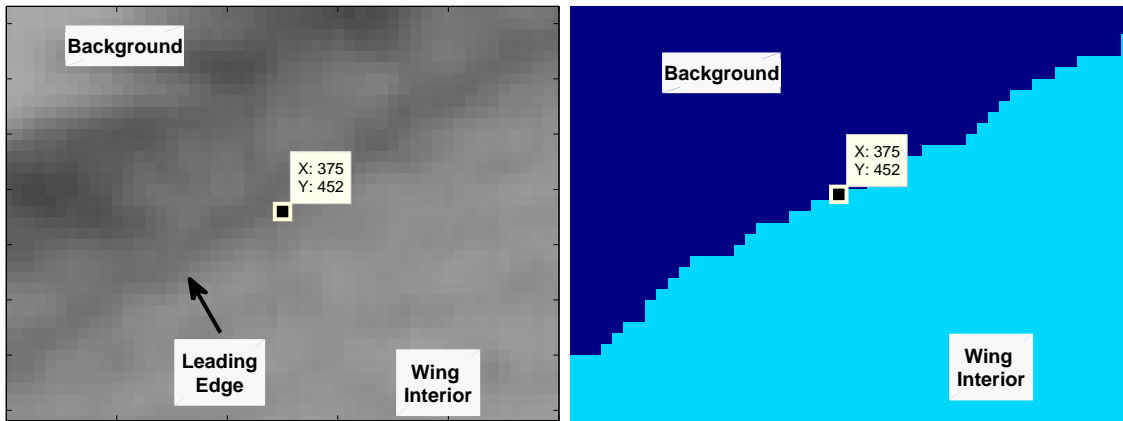


FIGURE 17: Frangi Segmentation leading edge placement. (left) Original image, and (right) Frangi segmentation. The segmentation locates the leading edge with high precision.

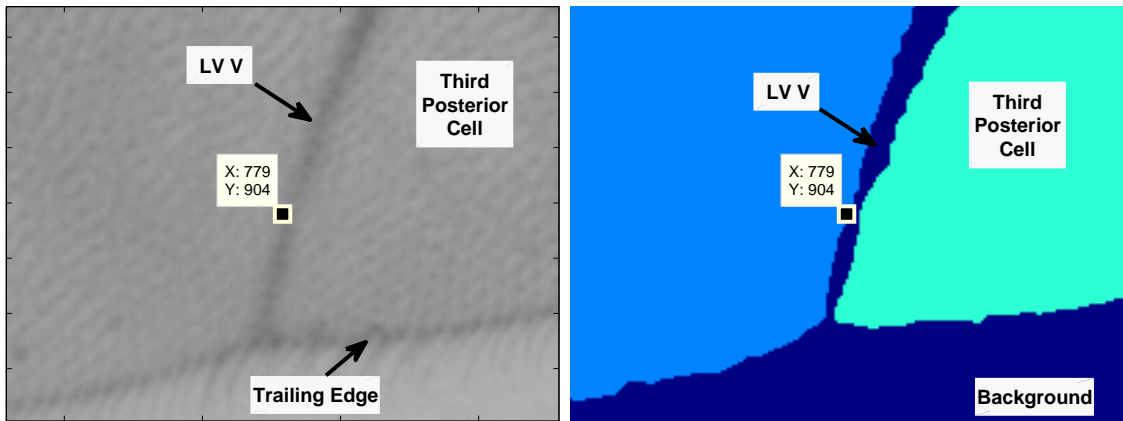


FIGURE 18: Frangi segmentation LV V placement. (left) Original image zoomed (right) Frangi segmentation zoomed. Longitudinal vein V near its intersection with the trailing edge is located with high accuracy.

is evident, due to the presence of dark striation filaments in the wing cell neighboring the trailing edge, as well as the method correcting for the underlying lack of contrast between the edge and its surroundings.

## CHAPTER 6

### IMAGE SEGMENTATION SUMMARY

The performance of the segmentation routines is measured by their ability to identify the wing boundaries and interior veins individually. For instance, if longitudinal vein V is not identified all the way until its intersection with the trailing edge, then it is considered to be not segmented. The anal crossvein and longitudinal vein VI are considered to be a single feature.

In addition to the three methods presented in this thesis (Adaptive Thresholding, Maximal Gradient, and Frangi Multi-Scale methods), the performance of a Level Set method (LSM) routine that was developed but not presented is also included. Level Set methods are a computationally intensive approach to dynamically evolving and tracking boundaries. Osher and Sethian introduced the Level Set method to propagate and track the movement of boundary curves, using canonical examples in flame propagation and crystal growth [13]. Fedkiw and Osher [14], Sethian [15], and Shu and Osher [16] provide ample background and theory for reference.

Table 2 reports the performance of each segmentation routine over the entire 48 wing image set. The routines were all run on a 2.1GHz Pentium processor with 4GB of RAM. Segmentation of several features is seen to be trivial, in that all methods identify the features. The leading edge, trailing edge, longitudinal veins III and IV, and posterior and anterior crossveins are always identified. Longitudinal vein II is always identified in every image for every segmentation routine, except for the Frangi method for a single image. The methods are distinguished by their ability to fully identify longitudinal vein V and identify longitudinal vein VI.

The Adaptive Thresholding method, the simplest method from a

mathematical perspective, finds longitudinal vein V in 42 of the 48 images. However, the method is only able to recover longitudinal vein VI in ten of the images. The Maximum Gradient method best identifies longitudinal vein V, fully finding it in 47 of the 48 images. The method also shows strong improvement from the Adaptive Thresholding routine in identification of longitudinal vein VI, although still fails to identify it in twelve images. The Frangi Multi-Scale method identifies longitudinal vein V almost as well as the Adaptive Thresholding method while achieving the best performance in identifying longitudinal vein VI. Despite its mathematical sophistication, the Level Set method was unable to materially improve on the performance of the Adaptive Thresholding method. Figure 19 shows a side by side comparison of the four segmentation routines performed on Wing30BIG. Longitudinal vein V is identified in all four routines. The Adaptive Thresholding routine fails to find longitudinal vein VI and as a result, the wing cell to the right of the vein is not included in the resulting segmentation of the third posterior cell. Longitudinal vein VI is identified in each of the other methods.

TABLE 2: Segmentation Methods Performance Comparison

<b>Number of Each Feature Identified in the Image Set per Method</b>					
		<i>Thresholding</i>	<i>Max Grad</i>	<i>Frangi</i>	<i>LSM</i>
<b>Time per Image</b>		6	10	19	1613
<b>Key Wing Features</b>	<b>Leading Edge</b>	48	48	48	48
	<b>LV II</b>	48	48	47	48
	<b>LV III</b>	48	48	48	48
	<b>LV IV</b>	48	48	48	48
	<b>LV V</b>	42	47	41	43
	<b>LV VI</b>	10	36	44	15
	<b>Trailing Edge</b>	48	48	48	48
	<b>Posterior CV</b>	48	48	48	48
	<b>Anterior CV</b>	48	48	48	48

Note: For each segmentation routine, the number of times in the 48 wing image set that a given wing feature was identified. Identification of many of the wing features is seen to be a trivial task, in that all methods identify the features across the entire image set. Full segmentation of longitudinal vein V and identification of longitudinal vein VI distinguish the performances of the segmentation routines. The times to segment are measured in seconds on a 2.1GHz Pentium processor with 4GB of RAM.

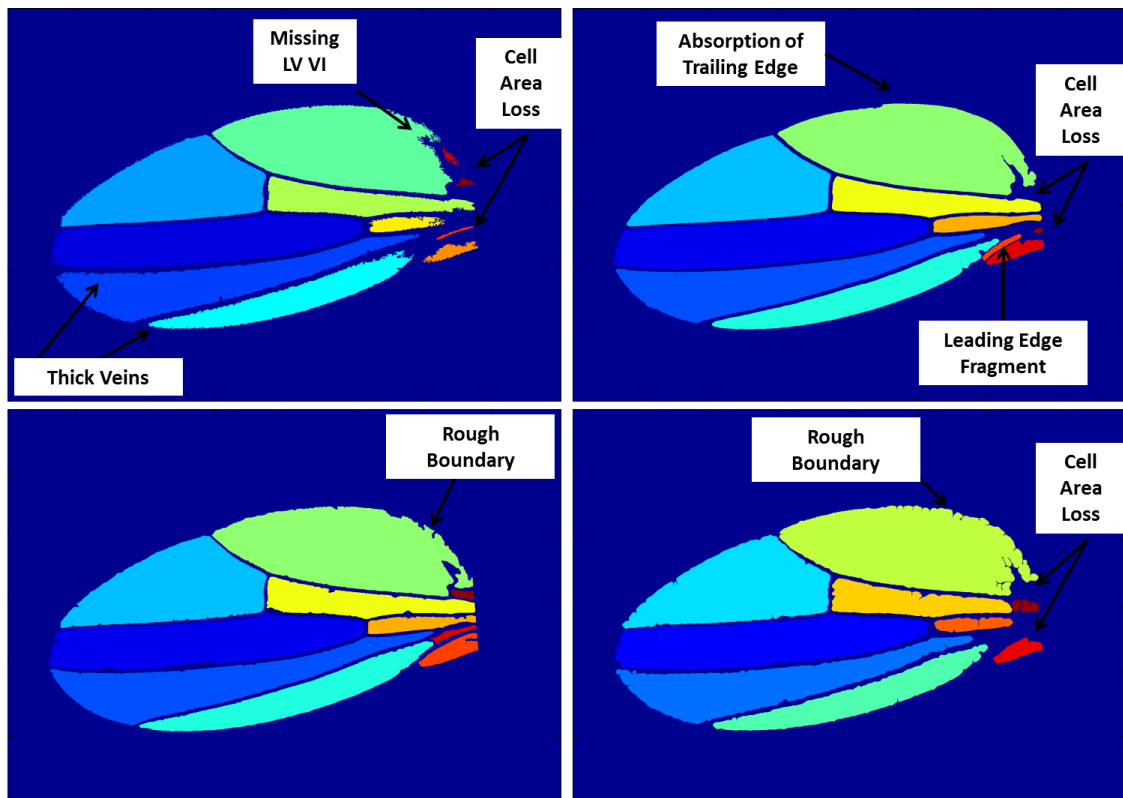


FIGURE 19: Annotated segmentation results comparison for wing30BIG. (upper left) Adaptive Thresholding, (upper right) Maximal Gradient, (lower left) Frangi, and (lower right) Level Set Methods.

However, variations in performance not captured by the performance measure, as elaborated for each method in their respective Chapters, are also evident in the side by side comparison in Figure 19. For reference, the original image raw and sharpened are shown in Figure 20. In the Adaptive Thresholding routine, smaller wing cell areas near where the veins converge fail to be identified. Excessive thickness of longitudinal vein II and III is evident, due to the distortion from inclusion of darker wing cell pixels in the vein segmentation necessary to identify longitudinal vein V along its entire length. This tradeoff also causes the loss of third posterior cell area and lack of identification of longitudinal vein VI. In the Maximal Gradient routine, a portion of the leading edge is identified as a distinct wing cell area. Portions of the leading and trailing edges are also absorbed in their neighboring wing cells, as evidenced by the kink in the boundary of the third posterior cell, creating error in placement of the exterior boundary. These errors

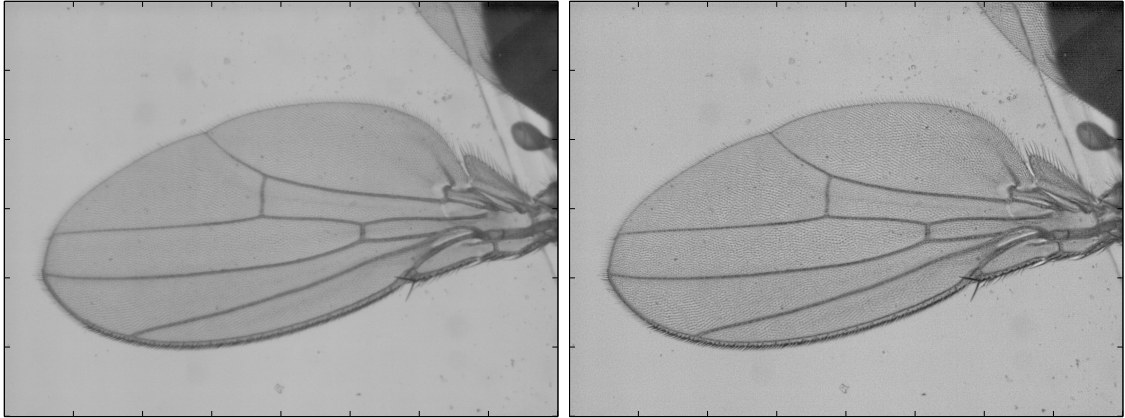


FIGURE 20: Original (left) and sharpened (right) wing30BIG image.

are caused by the method's inability to identify thick veins as single boundaries between cells. In the Frangi method, filaments of wing cell material which border the vascular network are included in the vein segmentation, which creates a roughness in cell boundaries. The Level Set result suffers from the same limitations as the Adaptive Thresholding result. The Frangi method segments 420 of the image set's total 432 key wing features, narrowly edging the Maximal Gradient method's 418 cumulative score. Additionally, the Frangi method has the fewest categories of segmentation error not represented in the wing feature score. Namely, a loss of smoothness along portions of cell boundaries. This effect would be alleviated if the Frangi segmentation results were to be incorporated in the existing asymmetry calculation process, since an intermediate step between segmentation and splining thins the vasculature to a single pixel thickness. The method also demonstrates the most ability to identify and retain small cell areas where the vasculature converges near the cut line. The Maximal Gradient method suffers, due to its retention of portions of the leading and trailing edges as either distinct cells or as area and boundary location distortions. As such, the Frangi method is the best of the surveyed methods for segmentation of the wing images, and an improvement upon current practices, for which the Adaptive Thresholding method is a proxy.

It should be noted that each of the routines is run with fixed parameters on

the entire image set, and not run individually on separate images with parameters tuned to each image. The goal is to automate the segmentation process, and manual tuning of parameters for each image is inconsistent with that goal. Since no routine was able to perfectly segment the entire image set, some parameter tuning could be endeavoured as a form of error handling after evaluation of the selected segmentation routine's results. The quality of the Frangi result would permit the least amount of parameter tuning, which should be avoided due to its potential to introduce variation across the image set in location of landmark points.

## CHAPTER 7

### PROPOSED MEASURE OF WING PAIR SHAPE ASYMMETRY

#### Introduction

The image segmentation is an intermediate step towards the ultimate goal of the analysis of the shape variation in fly wing pairs across the 48 wing image data set. The current shape measures for the wings are based on the distance between  $N$  landmark points of the wing, for some  $N$ . The landmark points generally correspond to locations of intersection of the longitudinal veins with the leading and trailing edges and the three crossveins. Subsets of all vein intersection points often form the set of landmark points, due to identifiable measurement error in location of a landmark point as well as the choice of asymmetry measure itself. For instance, in [2], the average distance of the two ends of the posterior crossvein to the intersection of longitudinal vein IV and the trailing edge is calculated for each wing. The simple difference of this calculation between the left wing and right wing forms a measure of *Directional Asymmetry* (DA) of the fly.

More complicated measures utilizing a larger set of landmark points are also calculated. For instance, where  $d(1, 2)$  is the distance between landmark points one and two, *left* and *right* refer to the left and right wings of a fly wing pair, and  $\text{avg}(d(1, 2)_{\text{left}, \text{right}})$  is the average of the distance between points one and two over the left and right wings of the wing pair, the measure *Scaled Mean Directional Asymmetry (SMDA)* for a given fly is:

$$\text{SMDA} = \frac{N!}{2((N-1)!)} \left[ \sum_{i=1}^{N-1} \sum_{j=i+1}^N \frac{d(i, j)_{\text{left}} - d(i, j)_{\text{right}}}{\text{avg}(d(i, j)_{\text{left}, \text{right}})} \right]$$

Several other wing pair asymmetry measures are also calculated from the distance between landmark points. *Unscaled DA(cent)* is the simple difference

between left and right wings of the square root of the sum of squared distances from each wing’s centroid to the wing’s set of landmark points. Rankings of the 24 flies in the data set on the basis of this measure are shown in column one of Table 3.

Table 3 also shows the fly wing pair asymmetry rankings for several other asymmetry measures. Fortunately, the ranking of a fly wing pair’s asymmetry is consistent across the various measures. Flies 9, 23, 19, 7 and 2 have the greatest DA (left-right), as seen in the first four columns of the Table. Note that the Fluctuating Asymmetry metrics (FA) *Unscaled FA* in column five and *Scaled FA* in column seven reflect the magnitude of their corresponding DA metrics *Unscaled DA* in column one and *Scaled DA* in column three, respectively. As such, the FA measures lose the left-right directional information contained in the associated DA measures. Flies 22 and 14 also exhibit relatively large *mean FA* measures, as seen in columns six and eight, in addition to the above mentioned wings.

TABLE 3: The Benchmark Wingpair Asymmetry Measures Rankings

	Low Measurement Error Area Euclidean Distance Asymmetry Rankings							
	Unscaled <i>DA(cent)</i>	Unscaled <i>Mean DA</i>	Scaled <i>DA(cent)</i>	Scaled <i>Mean DA</i>	Unscaled <i>FA(cent)</i>	Unscaled <i>Mean FA</i>	Scaled <i>FA(cent)</i>	Scaled <i>Mean FA</i>
	9	9	9	7	9	7	9	7
	23	19	23	9	23	22	23	22
	19	7	19	19	19	9	19	14
	2	23	2	2	2	19	2	9
	7	2	7	16	7	14	7	13
	12	16	12	15	13	23	13	19
	16	15	16	23	12	12	12	12
	15	1	15	1	16	13	16	10
	8	8	8	3	15	20	15	24
	24	4	24	13	11	10	11	23
	1	12	1	21	8	24	8	5
	18	6	18	6	20	21	20	18
	6	24	6	4	17	2	17	20
	4	3	4	8	21	5	21	3
	22	18	22	10	24	18	24	21
	10	13	10	12	3	16	5	16
	14	21	14	24	5	1	3	2
	5	10	3	18	1	3	1	1
	3	17	5	17	14	11	14	11
	21	14	21	20	10	6	10	17
	17	22	17	14	22	8	22	8
	20	20	20	11	18	17	18	6
	11	11	11	22	6	15	6	15
	13	5	13	5	4	4	4	4

The wing pair shape asymmetry analysis explored herein seeks to study the variation in wing shapes through an analysis of the variance structure of the image data set. Wing shape variation is necessarily one of the sources of variation in the wing image data set. Qualitatively, several other sources of variance in the wing image data set can also be posited: (a) Left vs. right images, (b) pose variation – angle of placement of wing in image frame, (c) illumination variation and other potential variations in photo capture, (d) wing cell striation variation, (e) occlusions and presence of unintended image inhomogeneities, and (f) detailed shape variation – size and shape of entire wing, size of each wing cell, and thickness of veins.

There may well exist other unidentified sources of variation as well. Since all possible sources of variation in the wing image data set must necessarily be expressed as variation in the spatial distribution of pixel intensity values, the fundamental requirement underlying the variance decomposition techniques developed in this paper is the effective separability of subsets of pixel intensity value variation as represented by the identified qualitative factors. To formulate a usable shape asymmetry measure from an image data set variance model, wing shape variance must necessarily be a separable form of variance in the data set.

It is well known that substantial pose variation alone strongly degrades the ability of the technique implemented herein to capture other dimensions of image set variation [17]. In order to isolate the shape variation between wing images, elements of pose variance are reduced where possible. The left vs. right variance is partially reduced by flipping the vertical dimension of the right image, and then both left vs. right variance and pose angle variance are significantly reduced via an intensity-based image registration, which aligns the images based on similar intensity value matching [18]. Wing5 is the reference wing image for alignment, due to its center position in the image frame and absence of occlusions or other extraneous data. Figure 21 shows Wing1 on the right before and after alignment to Wing5.

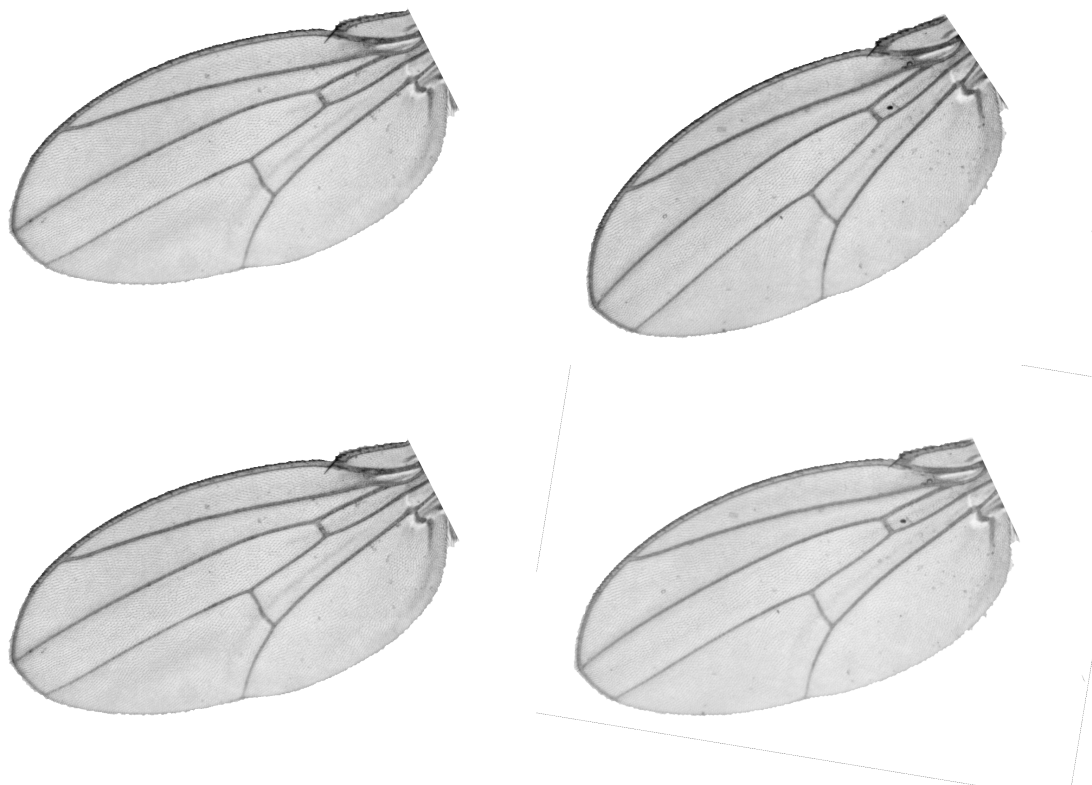


FIGURE 21: Reduction of pose variance through alignment. Alignment of Wing1 to Wing5: (upper left) Wing5, (upper right), Wing1 before alignment, (lower left) Wing5, and (lower right) Wing1 after alignment.

### Background Math: Singular Value Decomposition

Often in large data sets, there exists a lower dimensional basis which closely approximates the input data set. Dimension reduction of this nature enables accurate and efficient algorithms for identification, classification and prediction. The canonical tool of this form of data analysis is the *singular value decomposition* (SVD).

For any matrix  $A \in \mathbb{R}^{m \times n}$ , the SVD is a factorization that exists in the form of:

$$A = U\Sigma V^T \tag{7.1}$$

where  $U \in \mathbb{R}^{m \times m}$  and  $V \in \mathbb{R}^{n \times n}$  are both orthogonal matrices,  $\Sigma \in \mathbb{R}^{m \times n}$  is a diagonal matrix and the  $t$  symbol denotes the transpose. By definition, a square

matrix  $U$  is *orthogonal* if

$$UU^T = I$$

where  $I$  is the identity matrix of same size as  $U$ . An orthogonal matrix is always invertible and has the property of

$$U^{-1} = U^T$$

where  $U^{-1}$  denotes the matrix inverse.

The columns of an orthogonal  $m \times m$  matrix form an orthonormal basis for  $\mathbb{R}^m$ . Necessarily, then, for any two columns  $i$  and  $j$  of an orthogonal matrix  $U$ ,  $\langle u_i, u_j \rangle = 0$ , where  $\langle \cdot, \cdot \rangle$  denotes the dot product. In other words, the covariance of any two columns of an orthogonal matrix is zero. The columns of  $U$ , known as the *left singular vectors* of matrix  $A$ , represent the independent sources of variation contained in the entries of  $A$ . For a de-meaned matrix  $A$ , the scaled left singular vectors are also referred to as the *principal components* of  $A$ . The singular value decomposition can then be seen as a change of coordinates of matrix  $A$  into the dimensions of its independent sources of variation.  $A$  can then be rewritten as a linear combination of these independent sources of variation

$$A = \sum_{i=1}^r \sigma_i u_i v_i^T \tag{7.2}$$

where  $r$  is the rank of  $A$ ,  $v_i$  is the  $i$ th column of  $V$ , and the weightings  $\sigma_i$  are the non-zero diagonal entries of the matrix  $\Sigma$ .  $\sigma_i$  are known as the *singular values* of  $A$ , and its value represents the amount of variance explained by its associated left singular vector.

Each principal component can be evaluated for a physical interpretation of the variance of  $A$  that it contains. A physical interpretation of the principal component may not be apparent, or even exist at all. However, if a principal component represents a desired source of variance in the original data matrix, it

may be evaluated in isolation or in conjunction with other (and not necessarily sequential) principal components. The weightings on two principal components identified as meaningful are often shown as a scatter plot for a given set of input vectors (the columns of the original matrix  $A$  here), allowing for cluster analyses.

The other main utilization of the singular value decomposition is to form a low-rank approximation of the original higher dimension data. Low-rank approximations are useful to isolate and combine only the dominant sources of variance. By the Eckart-Young theorem [19], for a given  $z$ , with  $z < \text{rank}(A)$ , the best rank  $z$  approximation of  $A$  is the rank  $z$  linear combination of left singular vectors of  $A$  given in Equation (7.2) with  $r$  replaced by  $z$ , denoted  $A_z$ . Formally stated:

$$A_z = \text{argmin} \|A - B\|_F \quad \text{subject to } \text{rank}(B) = z \quad (7.3)$$

#### Isolation of Wing Shape Variation

In order to investigate variations in the overall shape of the wings, as opposed to the shape of each wing cell area as determined by both wing perimeter *and* the interior vascular network, a segmentation of the aligned wings as individual blobs was created in the Wing As Blob data set. In this data set, there is no variance for placement of the internal vasculature, nor illumination variation, wing cell striation variation across the data set, or pose variation, save for the possibility the segmentation result is contaminated by these factors. Since inability to perfectly align wings is itself a function of shape difference between wings, shape variation should be the dominant if not exclusive form of variance in the data set, since location of the perimeter of the wing blob exclusively determines shape.

A singular value decomposition of the data set yields the dimensionality of its variance structure. The relative magnitudes of the singular values of the 48 images in the Wing As Blob data set necessary to retain 95 percent of the set's variance are shown in Figure 22. The first PC contains 42% of the energy in the data. The first three PCs combined contain 58% of the energy, and the first five

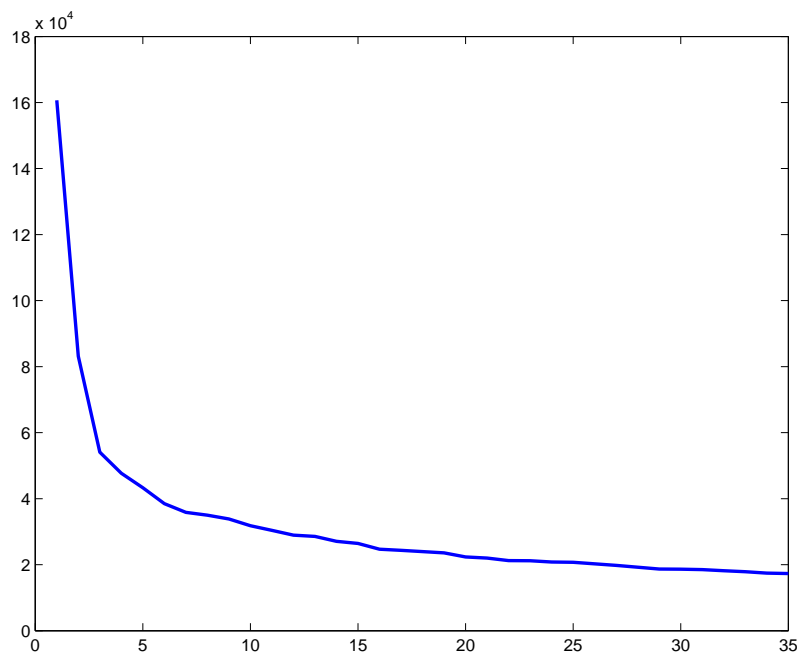


FIGURE 22: Wing As Blob data set singular values plot. A plot of the singular values obtained via an SVD on the centered Wing As Blob data set necessary to retain 95% of the set’s energy. The first PC contains 42% of the energy in the data. The first three PCs combined contain 58% of the energy, and the first five contain 65%.

contain 65%. Almost two-thirds of the variance in the data set is contained in the first five PCs. Since the data set was created to isolate shape variation from other sources of variation in the original image set, evaluation of the difference in contribution of the first several PCs between each wing in a wing pair should yield an asymmetry measure for the wing pair.

Two heuristics for investigation of wing shape variance are utilized:

(a) evaluation of the dominant principal components obtained via the SVD for shape features and comparison of the factor weightings (*i.e.*, PC coefficients) in each wing pair for these PCs and (b) construction of low rank wing approximations of various ranks for stochastic shape analysis. For instance, if the shape of a given wing does not change between rank 10 and rank 15 approximations, then it can be deduced that the principal components 11-15 do not contain discriminatory shape information. While much of the set variance is contained in the first five PCs, 95% of the set variance is not retained until the 35th PC, suggesting small changes in

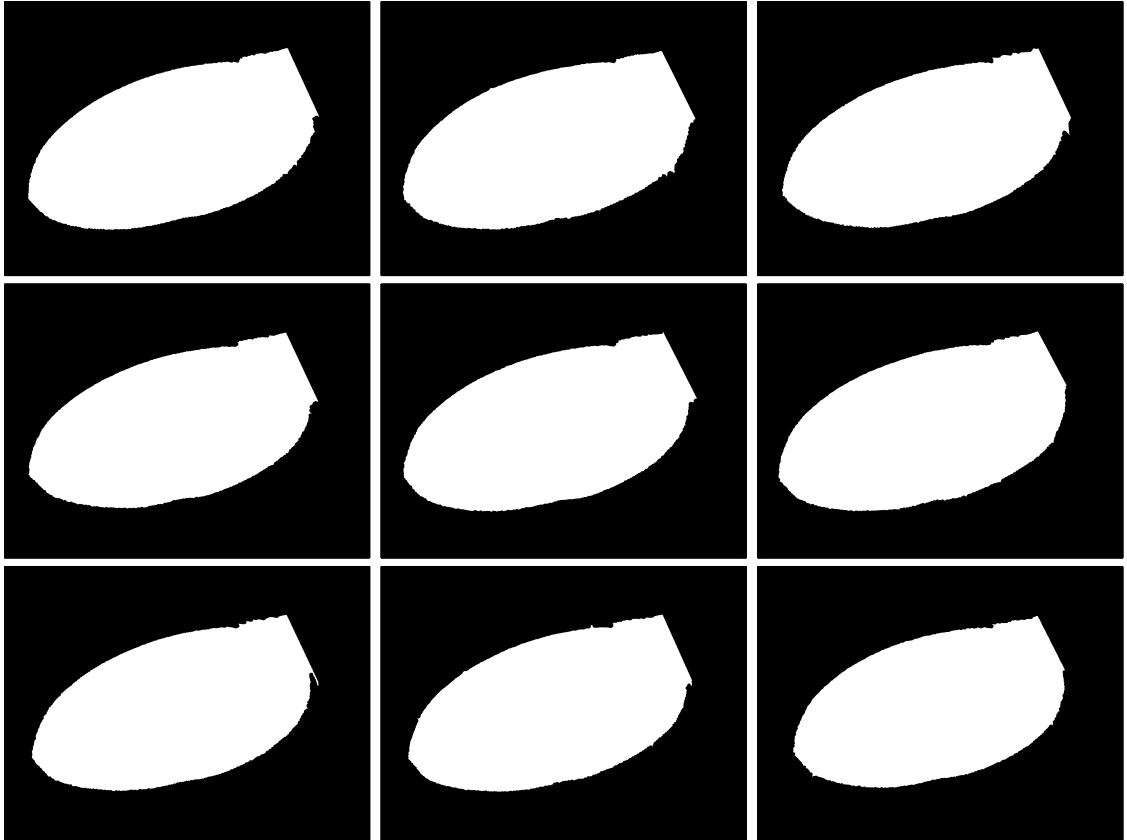


FIGURE 23: Aligned Wing As Blob wings 1 – 9

shape of the wing blobs are still being selected throughout the PC set, or the segmentation introduces spurious variance in wing shape, or both.

For reference, the first nine wings of the data set are displayed in Figure 23. The first nine principal components are displayed concatenated as a single plot in Figure 24. Each principal component itself visually appears as the boundary of a wing. Since the data was centered prior to performing the SVD, wing area common to all wings was in effect deleted from the set, leaving only variations in the boundary placement from wing shape asymmetries. Each PC evidently contains shape information, although each PC includes information on the placement of the boundary of the entire wing, precluding any feature by feature extraction. As such, a meaningful physical interpretation of the dimension of variance represented by each PC appears to be impossible.

While a meaningful physical interpretation of the PCs is unavailable, we do

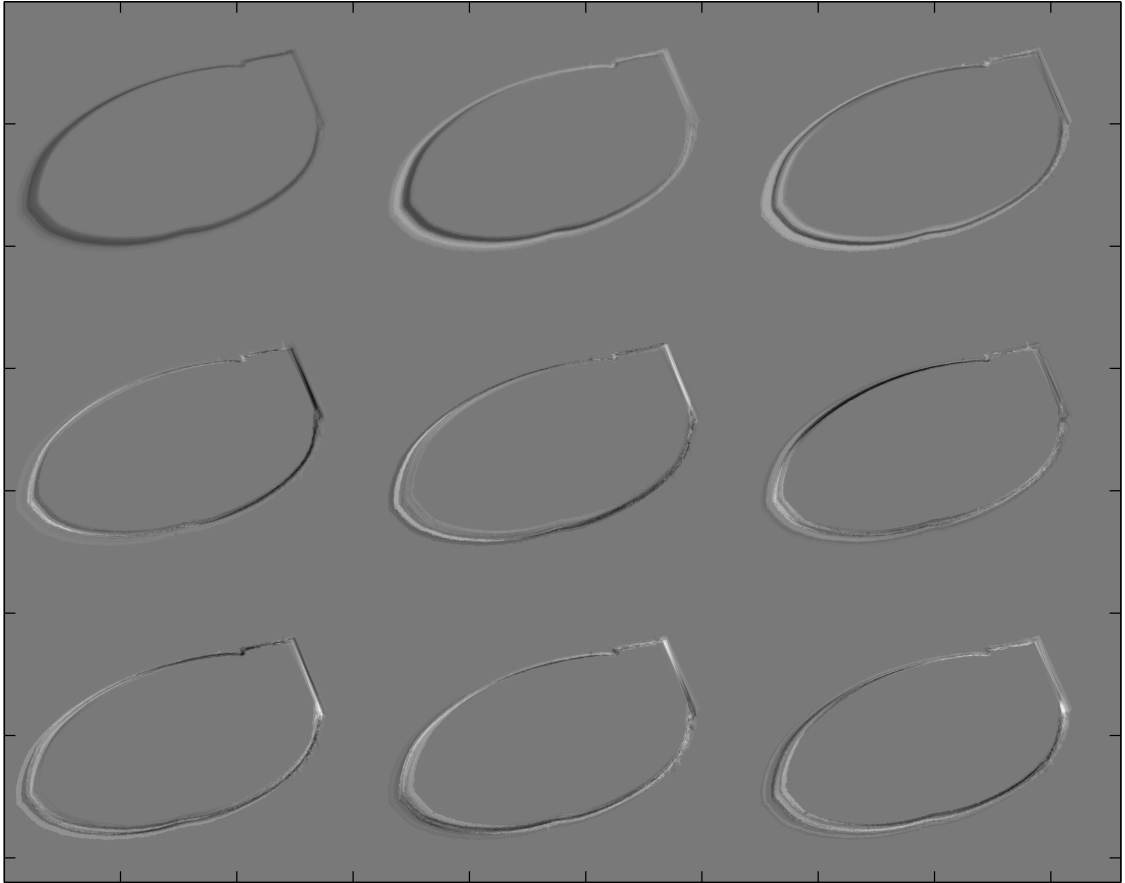


FIGURE 24: The nine PCs of largest explained variance. Each PC contains information on location of the wing boundary, and each visually appears to be the boundary of a wing, although a direct feature extraction appears impossible.

know that the relative contribution of each PC will be skewed towards the PCs of highest singular value magnitudes. This can be seen in Figures 25 and 26, which show most of the energy in approximations of Wing As Blob Wing5 and Wing6 images is contributed by the first three PCs, as expected by the magnitudes of the associated singular values. Still, other PCs contribute. Interestingly, Wing5 has greater contributions from PCs 5 and 6, while Wing6 has a greater contribution from PC4, while the contributions from the other PCs are not noticeably different.

#### Low-Rank Approximations

In order to allow for shape expressions to manifest at varying rank approximations across the wing image set, as well as to acknowledge the uncertainty in assigning a particular shape meaning to any of the PCs, a shape asymmetry measure is calculated on the assumption that the shape variance must

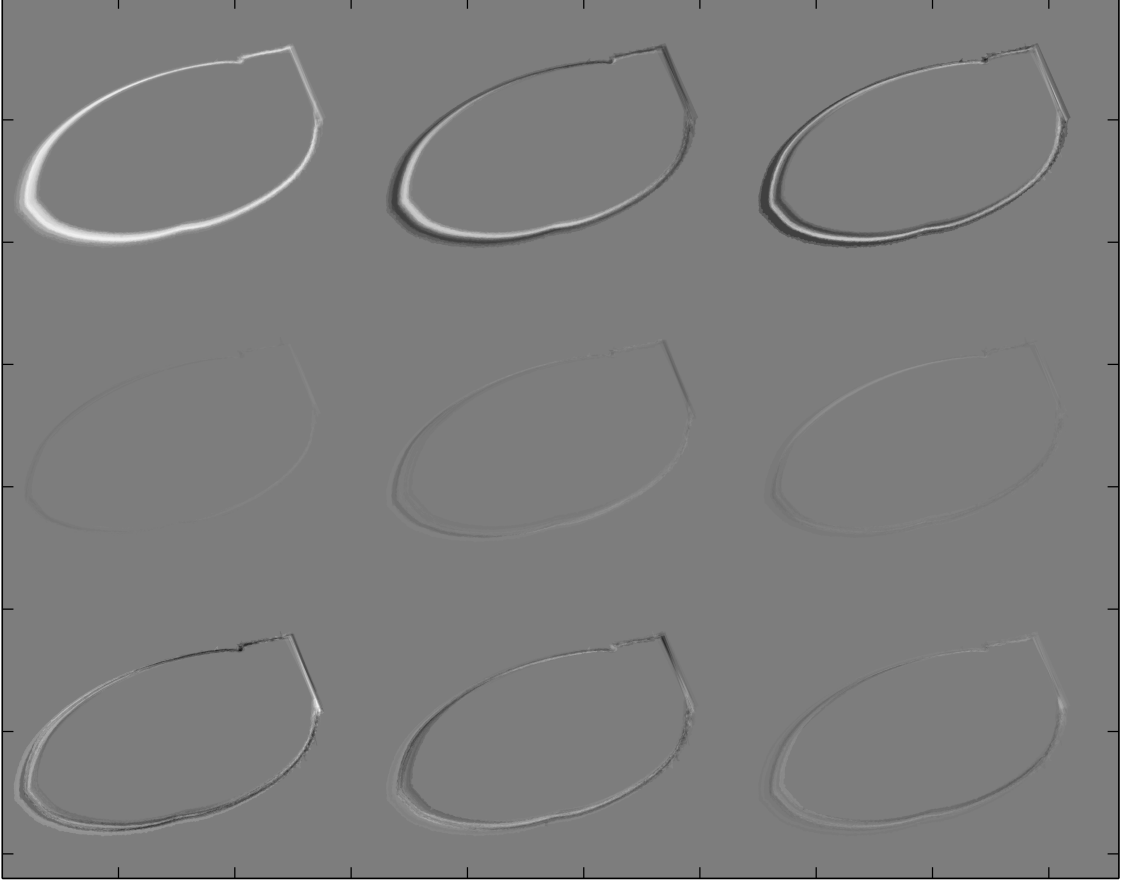


FIGURE 25: Contributions of PCs 1-9 to a low-rank approximation of wing5. Simple addition of each image yields a rank 9 approximation of wing5. The contributions of the first three PCs dominate, although shape effects are evident in the other PC contributions.

in fact be contained in the set of PCs, and thus for some  $N$ , shape variance for the entire image set will be captured in the rank  $N$  approximation. If shape asymmetry dominates other sources of variation in the set, then for some rank the asymmetry measure should reflect shape asymmetry. This measure is:

$$\text{Wingpair Shape Asymmetry Index} = \sum_{i=1}^N \sigma_i \times [V^T(i, \text{Left Wing}) - V^T(i, \text{Right Wing})] \quad (7.4)$$

Calculation of the wing pair asymmetry metric (WSAI) given by Equation (7.4) for the given  $N$  ranks is shown in Table 4. Flies 9, 7 and 2 maintain a ranking in the top four in left-right shape asymmetry for ranks 1 – 20, while fly 19 ranks sixth for ranks one and three, suggesting consistency with the benchmark

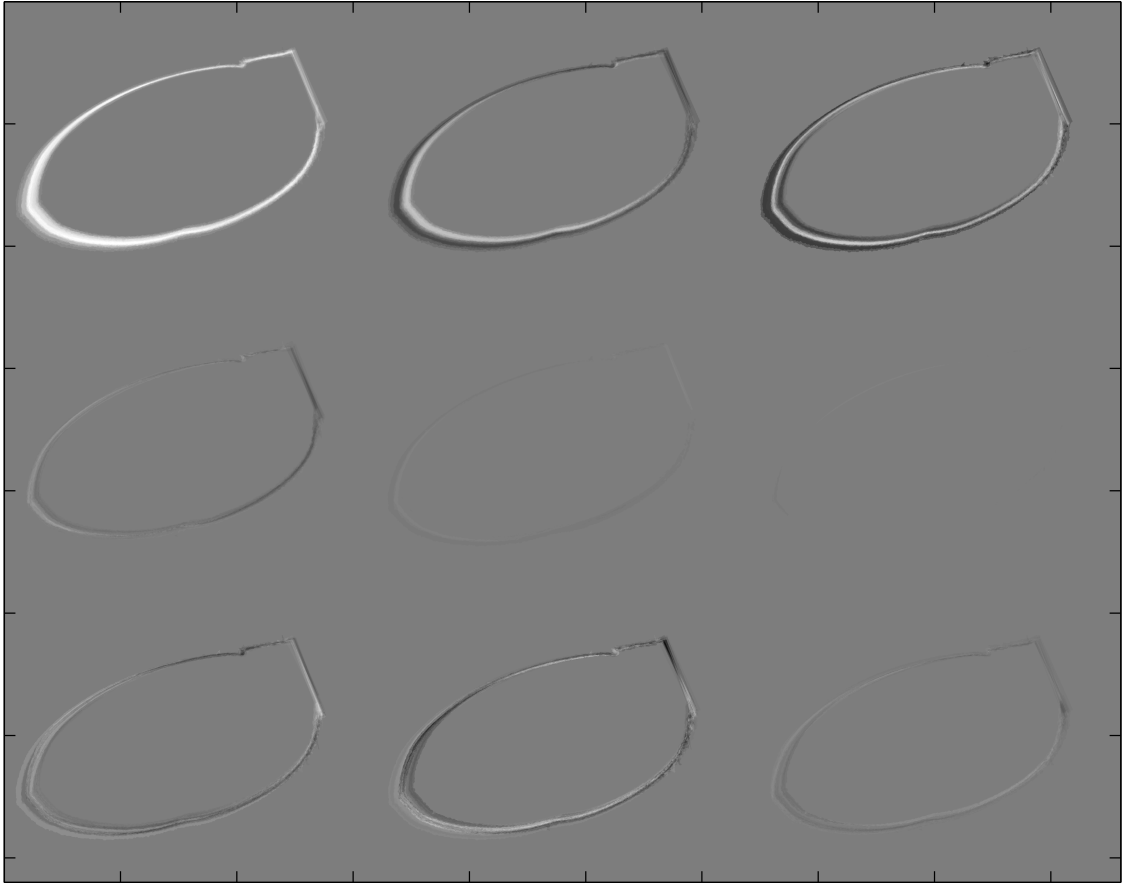


FIGURE 26: Contributions of PCs 1-9 to a low-rank approximation of wing6. Simple addition of each image yields a rank 9 approximation of wing6. The contributions of the first three PCs dominate, although shape effects are evident in the other PC contributions. The contribution of PCs 5 and 6 to wing6 are larger than their contribution to wing5, suggesting wing pair asymmetry is present in these PCs.

asymmetry rankings in Table 3. Further confirming the measure, WSAI identifies fly 11 as possessing the least left-right DA, in agreement with the benchmark measures, which place fly 11 next-to-last in Unscaled DA(cent), Unscaled Mean DA and Scaled DA(cent) in columns one through three. While the WSAI rankings are largely stable across lower rank approximations, using all 35 PCs necessary to retain 95% variance drops fly 7 down to sixth and fly 19 all the way to 22nd in asymmetry ranking, suggesting contamination from other sources of variance.

TABLE 4: Rankings of a New Measure of Wingpair Directional Asymmetry

		WSAI DA Measure Rankings											
		Fly Asymmetry Rankings at Rank N											
		<i>1</i>	<i>2</i>	<i>3</i>	<i>4</i>	<i>5</i>	<i>6</i>	<i>7</i>	<i>8</i>	<i>9</i>	<i>10</i>	<i>20</i>	<i>35</i>
<b>Fly Number</b>	9	9	9	9	9	9	9	9	9	9	9	9	
	6	7	6	6	6	6	6	6	6	6	6	6	
	2	6	2	7	2	2	2	2	2	2	2	15	
	7	2	7	2	7	7	7	7	7	7	7	2	
	21	21	21	15	15	15	15	15	15	15	15	16	
	19	20	19	21	21	21	21	21	21	21	17	16	7
	20	19	20	19	20	20	20	20	20	16	21	21	14
	24	24	24	20	16	24	19	16	20	16	17	17	17
	23	23	16	16	23	16	24	24	17	14	14	21	21
	16	16	3	24	3	23	16	23	24	24	23	23	23
	15	3	15	3	24	3	23	19	14	20	20	12	12
	3	17	23	23	19	19	3	3	23	23	24	20	20
	8	18	17	18	17	18	14	17	3	3	3	24	24
	13	15	18	8	18	17	17	14	5	18	12	4	4
	17	8	8	14	14	14	18	18	19	5	1	3	3
	5	5	5	1	5	8	8	1	18	4	18	1	1
	18	1	13	4	8	1	1	5	4	12	5	18	18
	4	4	4	17	4	4	12	8	12	1	4	13	13
	14	14	1	13	1	12	4	4	8	8	10	5	5
	12	12	14	12	12	5	5	13	1	19	13	10	10
10	13	12	5	13	13	13	12	13	10	8	8	8	
1	10	10	10	10	10	10	10	10	13	19	19	19	
22	22	22	22	22	22	22	22	22	22	22	22	22	
11	11	11	11	11	11	11	11	11	11	11	11	11	

Note: In the Wing As Blob data set, flies 9, 6, 2 and 7 maintain the greatest asymmetry in the lower rank approximations as determined from the measure Wingpair Shape Asymmetry Index (WSAI). The stability of the ranking over rank approximations, and agreement with the benchmark rankings, suggests wing shape variation is largely contained in a low dimensional subspace of the image set.

For comparison to the FA measures of Table 3, a measure of distance in PC coefficient space (*i.e.*, indifferent between left-right and right-left asymmetry) between the wing pair is explored. This is formulated as:

Wing Shape Asymmetry Index II =

$$\left( \sum_{i=1}^N \sigma_i \times [V^T(i, \text{Left Wing}) - V^T(i, \text{Right Wing})]^2 \right)^{1/2} \quad (7.5)$$

TABLE 5: Rankings of a New Measure of Wingpair Fluctuating Asymmetry

		WSAI II FA Measure Rankings											
		Fly Asymmetry Rankings at Rank N											
		<b>1</b>	<b>2</b>	<b>3</b>	<b>4</b>	<b>5</b>	<b>6</b>	<b>7</b>	<b>8</b>	<b>9</b>	<b>10</b>	<b>20</b>	<b>35</b>
<b>Fly Number</b>	11	11	11	11	11	11	11	11	11	11	11	11	11
	9	9	9	22	22	22	22	22	22	22	22	9	22
	22	22	22	9	9	9	9	9	9	9	9	22	9
	1	10	13	15	15	15	15	15	15	15	15	19	19
	6	13	10	6	6	6	6	6	6	6	19	6	15
	10	6	6	13	13	13	13	13	13	14	6	15	6
	2	12	2	14	14	14	14	14	14	13	13	1	1
	12	2	12	10	10	10	10	10	10	1	14	14	14
	7	1	1	1	1	1	1	1	2	2	1	13	13
	14	14	14	12	12	12	12	12	12	10	17	7	17
	4	7	7	2	2	2	19	1	12	2	12	12	12
	18	4	4	7	17	17	2	19	19	10	17	17	10
	5	18	18	4	7	7	17	17	5	12	10	5	5
	17	17	17	17	4	4	7	5	17	5	5	7	7
	21	5	5	18	19	19	4	7	4	4	2	2	2
	13	15	15	5	5	5	5	4	7	7	8	24	24
	19	19	19	19	18	18	18	8	8	8	21	8	8
	20	20	21	8	21	21	8	18	18	20	4	21	21
	8	21	8	23	8	8	21	21	21	18	23	4	4
	3	23	23	16	20	20	20	20	20	21	24	23	23
24	24	20	21	23	24	23	24	23	3	16	16	16	
23	8	24	3	16	23	24	23	24	23	20	20	20	
16	3	16	20	3	16	3	3	3	24	18	18	18	
15	16	3	24	24	3	16	16	16	16	3	3	3	

Note: Instability in the rankings over increasing rank approximations, and failure to agree with the benchmark FA rankings at any rank, indicate FA is not captured by Wingpair Shape Asymmetry Index II (WSAI II).

The asymmetry rankings produced by the measure are shown in Table 5. Flies 11, 9 and 22 have the greatest FA as measured this measure (WSAI II). Fly 9 has the most Unscaled FA(cent) and Scaled FA(cent) in the benchmark rankings, though flies 11 and 22 do not rank highly in either measure. As such, there is only very weak validation for WSAI II as an alternate FA measure.

#### Comparison of the Directional Asymmetry Measures

Moving beyond a comparison of the ranking of the flies in the WSAI measure and the benchmark DA asymmetry measures, we examine the actual quantities of the measures of each fly. We select Unscaled DA(cent) as the benchmark measure and rank five of the WSAI measure for the comparative analysis. Each measure is normally distributed around a mean very near zero, enabling us to translate each measure into a z-score expressing each fly's asymmetry in standard deviation units for both measures. Given the near zero means, positive z-scores indicate positive asymmetry as determined by the given measure, and larger z-scores reflect larger calculated asymmetry. Figure 27 (left) shows a scatter plot of the z-scores of each fly for the two asymmetry measures. Correlation between the two measures is good, with  $r = .5078$ . However, there are outliers which reduce the goodness of fit. In order to understand the discrepancy in identified asymmetry between the two measures, sensitivity analyses of each measure are endeavored.

#### Unscaled DA Sensitivity Analysis

A sensitivity analysis of the Unscaled DA measure demonstrates a high sensitivity to exact placement of the landmark points from the thresholding segmentation and splining procedure in *WINGMACHINE*. The existence and interaction of several factors can create variable boundary and vein location either outright (in relation to true location), in relation to other boundaries in the same image, or in relation to location of the same boundary in other images. The images on which the benchmark rankings are based are downsampled by a factor of five in each dimension. As such, one pixel of the lower resolution data equals an area of

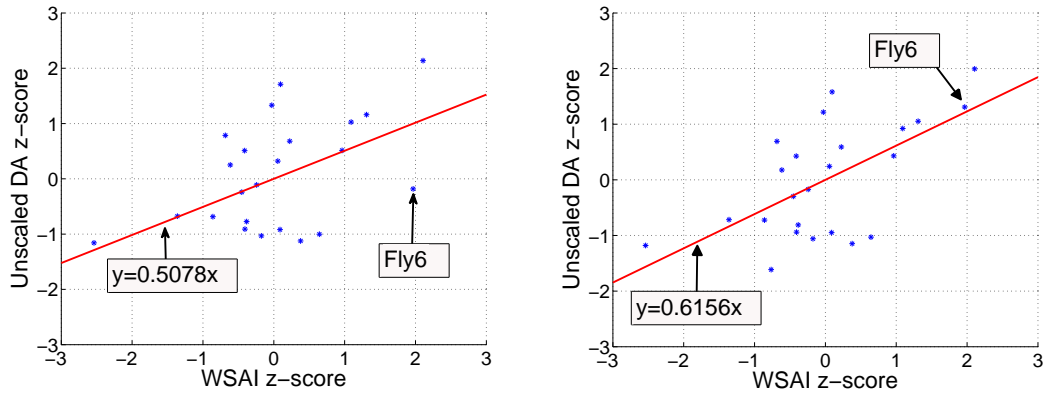


FIGURE 27: Scatterplots of WSAI and Unscaled DA z-scores for the 24 flies. (left) There is a 0.5078 correlation between the two measures of asymmetry. (right) After correcting fly 6’s landmark points 1-4, the correlation between the two measures has risen to 0.6156.

25 pixels in the original data. Although any downsampling will produce artifacts, the mosaic patchiness of the lower resolution images indicates use of a nearest neighbor downsampling, which is well known to introduce the most artifacts of all interpolation routines [20]. For instance, the location of thin veins (portions of the trailing edge and longitudinal vein V are only five pixels thick or less in the high resolution images) can easily be placed plus or minus one pixel in resizing, depending on the intensity values of neighboring regions. Neighboring regions in the image may be close in intensity values (cell striations) or even darker (cilia). This effect is not uniform because of variable proximity of features to these confounding elements. The replacement of a darker vein pixel with a lighter neighboring pixel in the downsampling has a knock-on effect in the segmentation procedure, because of the interaction with the thresholding parameter needed to identify veins fully. When portions of thinner veins disappear in the downsampling and are replaced with a higher intensity value from a neighboring region, in order to recover the vein a more relaxed intensity value thresholding level must be used, which in turn exaggerates thickness of other veins. Then the skeletonizing procedure will produce an error in location of the thicker vein.

The segmentation procedure which identifies the veins on which to apply splines to produce the locations of landmark points has several error potentials.

There is a smoothing filter in a preprocessing step which can itself move the boundary. Thinning the veins to produce single pixel thick veins on which to spline can also move the location plus or minus a pixel. Additionally, when splining results are determined to be strongly erroneous, the thresholding segmentation is repeated with individual parameter tunings for those wings - the size of smoothing filter to reduce image variability, the threshold intensity value to classify vasculature, and the size of structuring element in morphological operations to reduce extraneous image objects and smooth the vasculature chiefly among them. Each of these in isolation and in conjunction can easily move a boundary location in a wing image either absolutely or relative to another wing with a different set of parameters.

Fitting the identified veins with cubic b-splines also produces error. WINGMACHINE uses an *a priori* model of wing shape to place spline control points on and around the vein segmentation. The splining procedure optimizes the brightness of the pixels under the splines, in order to attract the splines to the vein segmentation. The splines are evolved by a gradient ascent routine over an energy field derived from smoothed pixel intensity values of the image segmentation. The routine often converges to an erroneous solution and mis-identifies the landmark point locations on which the asymmetry measure is calculated [21]. The spline errors are evaluated via visual inspection, and error correction is performed manually, although there is discretion in error tolerance. Errors in location of landmark points may survive the correction process, due to error tolerance or error in manual adjustment. In the data set studied here, the calculated locations of landmark points can vary from their true location. Figure 28 shows the location error of a sample point. The location of this point in the splining procedure is 2.83 pixels away from its true location in the lower resolution image.

Finally, the scale of the calculation is small relative to the measurement increments. Distances and asymmetries are being calculated in the fractions of a pixel, often with asymmetry between two wings less than a single pixel in distance.

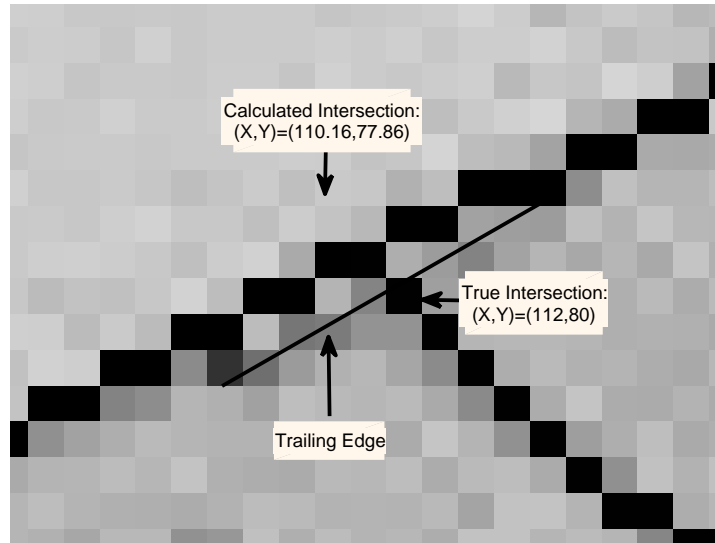


FIGURE 28: Landmark point location error. The thresholding segmentation and splining procedure to determine landmark point locations produces errors. Wing6 landmark point one is shown. The location is 2.83 pixels away from the landmark point location in the low resolution image.

Landmark points are located with sub-grid specificity in the splining procedure, which is false precision. The range of Unscaled DA(cent) in the data set is from 2.6 to  $-1.35$  pixels. The average Unscaled DA is only 0.34 pixels. 16 of the 24 flies have Unscaled DA magnitudes of less than one pixel. Intuitively, total measurement error appears to be of potentially larger magnitude than the quantity the calculation is measuring.

Since fly 6 has the greatest difference in z-score between the two calculations, we select it for further analysis. It has the second most DA in the WSAI calculation, and a corresponding z-score of 1.966. Additionally, it maintains a high WSAI across all rank approximations. Fly 6 ranks only thirteenth in Unscaled DA(cent), however, below the median, with a z-score of  $-0.188$ .

The locations of the wing pair's landmark points one through four, which correspond to the intersections of longitudinal veins V, IV, III and II with the trailing and leading edge, respectively, are manually evaluated and relocated by zero to two pixels each. As a result, the fly's Unscaled DA measure increases from

0.15 pixels to 1.84 pixels, which gives it the third highest Unscaled DA in the data set. A scatter plot of the updated Unscaled DA measure against WSAI is shown in Figure 27 on the right. Changing just four landmark points for a single fly increases the correlation between the two asymmetry measures to  $r = .6156$ .

#### WSAI Sensitivity Analysis

Using a rank five approximation for evaluation of asymmetry in WSAI ignores any shape effects of PCs of lower explained variance. And these PCs do contain shape information. This can be seen by tracking the location of a boundary point of a wing at a fixed horizontal coordinate over increasing rank approximations of the wing. We select a perimeter point of Wing9 for evaluation of the trailing edge location over the sequence of ranks 1, 5, 15, 25, 35, and 45. Table 6 shows the intensity value for the given row (Y) coordinate at column (X) coordinate 828, which, for orientation, is located just east of the intersection of longitudinal vein V along the trailing edge. The data in column one is presented visually in Figure 31. Utilizing the original image intensity value which signifies a wing blob pixel, 255, the boundary of the wing occurs at Y coordinate 912 in its rank 1 approximation. The wing is surrounded by (at least) five progressively darker halo rings which extend to Y coordinate 965. In a rank 5 approximation of the wing, the boundary remains at Y coordinate 912. In a rank 15 approximation, the boundary location has moved south of Y coordinate 916. From rank 25 through rank 45, Y coordinate 923's intensity value rises to 251, approaching eventual inclusion in the wing blob. The wing border ultimately extends to Y coordinate 926. In total, the wing boundary moved fourteen pixels over the sequence of increasing rank approximations, and all of that movement was caused by the inclusion of the lower explained variance PCs 6-48. The boundary movement is shown visually in Figure 29 against a zoom of the original wing blob region. This suggests there is a limit to the accuracy of low-rank measures of wing asymmetry.

The boundary location necessarily moves by adding the contributions of additional PCs, since each PC contains information about the placement of the

entire boundary, as seen in the plot of the first nine PCs in Figure 24. This remains true throughout the PC set. The contribution of any one PC to the wings is not of equal magnitude, as can be seen in Figure 30, which shows the contributions of the first three PCs for each of the 48 wings. Low rank measures of wing pair asymmetry can be contaminated by the consequent variable rates of convergence of the wing boundaries across the wing pair to the full rank (original) wing image boundary location. However, the variable rate of convergence between wings in a wing pair does manifest in the proposed shape asymmetry measures, since the only distinction between the wings at any rank approximation are the varying contributions of each PC to the rank approximations of the wing pair. This is exactly what the WSAI measure is calculating. The stability of the determination of the most and least DA flies in the set over ranks 1 through 20 suggests the measure is robust to inclusion of a vast majority of the image set variance. The general coherence of the WSAI rankings to the benchmark rankings for low rank approximations through rank 20 suggests shape asymmetry is largely contained in the PCs of highest explained variance and noise is contained in the PCs of lowest explained variance.

TABLE 6: Evolution of Wing As Blob Wing9 Trailing Edge Location

		Vertical Intensity Value Profiles at Rank N					
		<i>1</i>	<i>5</i>	<i>15</i>	<i>25</i>	<i>35</i>	<i>45</i>
Y Coordinate	<b>912</b>	<i>255.0</i>	<i>255.0</i>	255.0	255.0	255.0	255.0
	<b>916</b>	223.7	198.5	<i>273.5</i>	<i>275.1</i>	261.2	256.8
	<b>925</b>	122.3	54.5	127.9	192.4	<i>258.2</i>	<i>255.5</i>
	<b>935</b>	34.5	(63.5)	16.5	(8.9)	(28.5)	(10.8)
	<b>945</b>	(43.7)	18.8	14.5	17.8	(6.7)	(1.1)
	<b>965</b>	(7.6)	2.1	(1.3)	(2.8)	0.2	(0.1)

Note: Application of a 255 Intensity Value Inclusion Test for Determination of the Wing Boundary at Pixel X Coordinate 828. The intensity values of six Y coordinates for the given X coordinate are tracked over increasing rank approximations of the wing. An intensity value of 255 or greater indicates the pixel is interior to the wing boundary. The location of the boundary evolves as the rank of the wing blob approximation is increased, demonstrating that PCs of lower order contain shape information. The italicized font indicates the wing boundary location in the given rank approximation. The data in column one is expressed visually in Figure 31. The placement of the boundary location at each rank approximation, as denoted by the red font in each column, is shown visually in Figure 29.

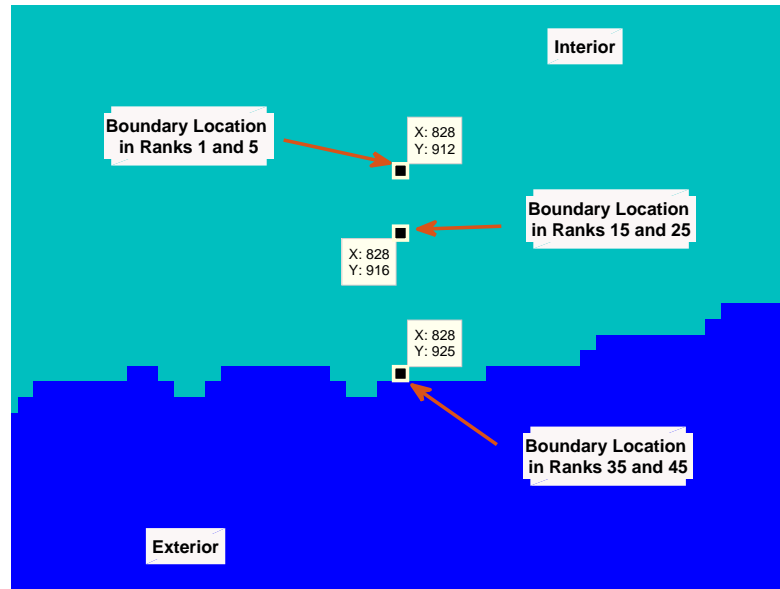


FIGURE 29: An illustration of the shape effects of PCs of lower explained variance. A pixel intensity value threshold test is applied to determine vertical location of the wing boundary at a fixed horizontal coordinate along the trailing edge. Application of this test over increasing rank approximations of the wing image demonstrate that the locations of boundary points evolve over increasing rank approximations. Since the placement of all boundary points determines wing shape, the shape of the wing is evolving over increasing rank approximations.

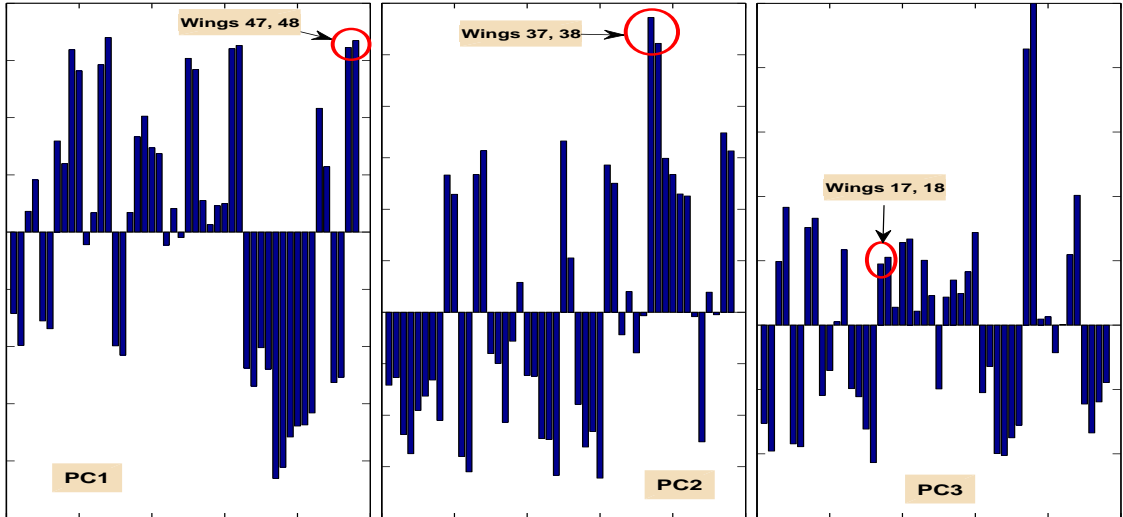


FIGURE 30: Contributions of the first three PCs to the Wing As Blob wing set. The coefficients show wing pair coherence in contributions of the PCs.

### Further Work

Several versions of the image data set were created to investigate the effects of image variance reduction concepts on the separability of wing shape variance. These techniques included: (a) image background standardization, (b) batch alignment to Wing5, (c) batch alignment to Wing5 followed by wing pair-wise alignment, (d) application of an averaging filter to reduce striation variation, (e) isolation of the low measurement error area portion of the wings, (f) reductions in image size, (g) Frangi segmentations of the wings, and (h) isolation of the sparse error in each wing image via robust PCA.

Applying the same shape asymmetry analysis heuristics to these data sets do not produce more favorable results. The greater amount of shape information, including shape of individual wing cells, as well as the more pronounced presence of the other sources of variation as detailed in Chapter 7 frustrate the attempt to isolate shape variation in the wing image sets. Interestingly, Birdsall et al. report the shape of each wing cell region is independently controlled at the genetic level [6]. For our purposes, none of the data sets contain low dimensional variance structures. Fly 19 is still identified as possessing the most DA, and fly 11 possesses the least DA, as measured by WSAI in other data sets, in conformance with the

benchmark rankings. However, the coherence of WSAI rankings to the benchmark is otherwise low.

### Summary

The new WSAI measure has been shown to correlate positively with the benchmark Unscaled DA(cent) measure, confirming the measure as containing shape asymmetry information. Both measures agree on the asymmetry of the most DA asymmetric wings, both of highest and lowest left-right asymmetry. Both measures identify the population of 24 flies as possessing mean DA of very close to zero. Both measures are normally distributed about their means. The measures differ mainly on the exact magnitude and ranking of DA in flies with measured DA within one standard deviation of the mean. However, the error magnitude in the benchmark measure has been shown to be of larger magnitude than the identified difference in DA between the two measures.

In any event, the two measures should not be expected to perfectly correspond. The benchmark asymmetry measures essentially measure the variation in the shape of the n-gon with vertices at the low measurement error landmark points, while WSAI measures variation in placement of the entire wing boundary. Variations in the wing boundary away from the landmark points are not captured by the benchmark asymmetry measures, for instance the amount of and distribution of curvature of the trailing edge between landmark points one and two.

Both measures have been shown to have measurement errors of similar magnitude. The difference in approaches suggests the error-generating processes are independent. DA measures assume that the n-gon variation reflects wing shape variation, and that the true asymmetry outweighs the errors in the measurement procedure. WSAI assumes that the majority of each wing's shape information is contained in a low dimensional subspace of the wing image set and can be recovered from low-rank approximations using the dominant sources of variance in a blob segmentation of the wing, disregarding the shape information contained in PCs of lower explained variance. Further study is required to determine if these

errors are correlated, or if the measures can serve as complements with independent errors. From this perspective, the positive but not perfect correlation suggests the errors are not materially related.

There is an impediment to this error analysis, however. Even if the locations of the entire vasculature network including the exterior boundary were known with absolute certainty from expert identification, the question becomes what to do with that location data. In order to do an error analysis of the distance based asymmetry measures or the WSAI measure, there must exist some objective ‘true’ scalar measure of shape with which to compare. This does not yet, nor may ever, exist. Small-scale shape variations in objects of similar overall shape may prove to be irreducibly high-dimensional. In the interim, WSAI can be implemented as a complementary asymmetry measure, to confirm the relative magnitudes and rankings of asymmetry based on the Euclidean-distance between landmark points. Perhaps with pseudo-data of known properties the various measures of shape asymmetry can be better assayed.

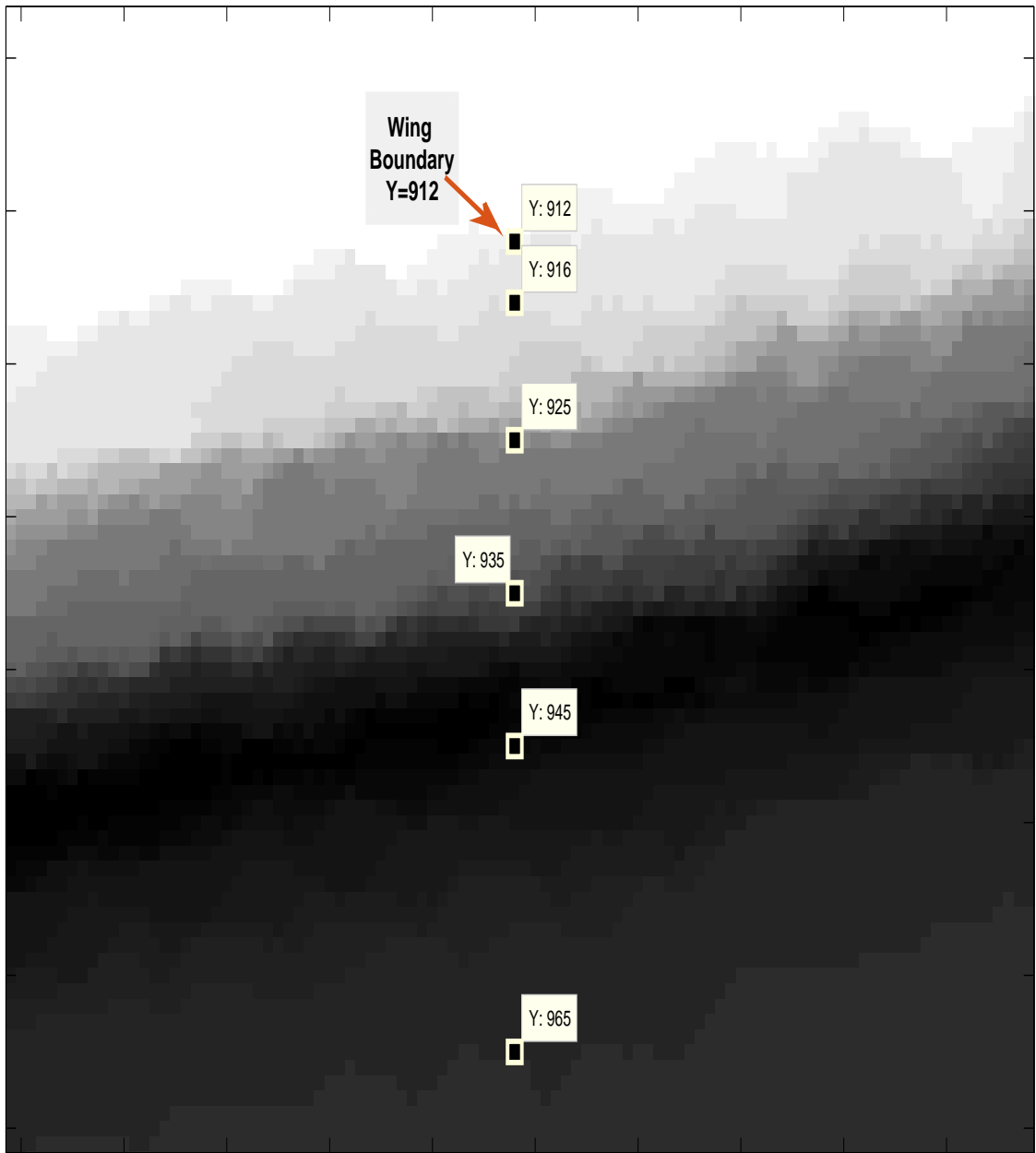


FIGURE 31: Wing As Blob wing9 rank 1 approximation southern edge zoom. Application of an intensity level threshold test yields vertical (Y) coordinate location of the wing boundary at horizontal (X) coordinate 828. The Figure is a visualization of column one of Table 6. The halo shadowing around the boundary is a feature of the first PC.

## APPENDICES

APPENDIX A  
MATLAB CODES

```

1 function [imgout1, imgout2]=FrangiCallSharpImg(img,binarythresh,areathresh)
2 %takes input image IMG and sharpens it with a TOPHAT BOTTHAT procedure
3 %before passing it to FRANGI.
4 %converts the Frangi output image to binary with input BINARYTHRESH
5 % labels connected components and eliminates small objects with area
6 % beneath input AREATHRESH
7 % recommended values: BINARYTHRESH: .01, AREATHRESH 500
8 % outputs are labeled images IMGOUT1 and IMGOUT2, which differ in only that
9 % IMGOUT2 has had a combination of morphological operations to
10 % reconstitute area lost to the FrangiCallSharpImg preprocessing steps
11
12 % sharpen input image and convert to double format for frangi filter
13 se=strel('disk',5);
14 g=img+imtophat(img,se)-imbothat(img,se);
15 g=double(g);
16
17 % Frangi set with paramters: sigma range 1:10, 'FrangiScaleRatio', 2,
18 % 'FrangiBetaOne', 0.65, 'FrangiBetaTwo', 20
19 [outIm,whatScale,Direction] = FrangiFilter2D(g);
20
21 %convert output to binary image
22 outImBinary=im2bw(outIm,binarythresh);
23
24 %label the remaining wing subregions
25 [L]=bwlabel(outImBinary);
26 %apply an area thresholding to eliminate extraneous data
27 s = regionprops(L, 'Area');
28 area_values = [s.Area];
29 idx = find((area_values>=areathresh));
30 bw2=ismember(L,idx);
31 % label and compute stats of the remaining subregions of interest
32 [LL]=bwlabel(bw2);
33
34 % light connectivity enhanmcements
35 % connect vein segments 1 pixel apart
36 LLbridged=bwmorph(LL,'bridge');
37 [LLB]=bwlabel(LLbridged);
38 LLBcomp=imcomplement(LLB);
39 % small opening
40 se=strel('disk',1);
41 L1pre=imopen(LLBcomp,se);
42 L1=imcomplement(L1pre);
43
44 %still need to help the frangi filter find the exterior boundary
45 image=double(img);
46 imagel=image;
47 [minlocation,peaks] = multipeaks(image);
48
49 %find exterior boundary
50 imagel(imagel>minlocation)=255;
51 imagel(imagel<=minlocation)=0;
52 imagelcompa=imcomplement(imagel);
53 imagelcomp1=im2bw(imagelcompa);
54 %erode cilia
55 imagelcomp=imerode(imagelcomp1,strel('disk',2));
56 % find wing blob
57 L = bwlabel(imagelcomp);
58 s = regionprops(L, 'Area');
59 area_values=[s.Area];
60 maxarea=max(area_values);
61 idx=find(area_values==maxarea);
62 imagelbdy = ismember(L, idx);
63
64 % find wing perimeter
65 imageperim=bwperim(imagelbdy);
66 imageperim=bwmorph(imageperim,'thicken',5);
67 imageperim=imdilate(imageperim,strel('line',3,0));
68 imageperim=bwmorph(imageperim,'bridge');
69 imageperim=bwmorph(imageperim,'fill');
70 L = bwlabel(imageperim);
71 s = regionprops(L, 'Area');

```

```

72 area_values=[s.Area];
73 maxarea=max(area_values);
74 idx=find(area_values==maxarea);
75 finalbdy = ismember(L, idx);
76 %frangi segmentation of veins and exterior boundary
77 frangiOut=L1+finalbdy;
78 frangiOut=im2bw(frangiOut);
79 % imgout1 is labeled image, ss are stats of the labeled objects
80 % imgout2 is labeled image after area repair, sss its stats
81 [imgout1, imgout2] = processbinaryedgeseg(frangiOut, 500,1);
82 [cutimage1] = cutpointmask(imgout2,k); %k is img #
83 % cell smoothing
84 [LL NN]=bwlabel(cutimage1);
85 idxcell=cell(NN,1);
86 se1=strel('disk',3);
87 se2=strel('disk',3);
88 LSMout=logical(zeros(size(LL)));
89 for i=1:NN
90     temp=logical(zeros(size(LL)));
91     temp(LL==i)=1;
92     temp=imdilate(temp,se1);
93     temp=imerode(temp,se2);
94     temp=imfill(temp,'holes');
95     idxcell{i}=temp;
96     LSMout=LSMout+temp;
97 end
98 tm=LSMout;
99 tml=bwmorph(tm,'thicken',2);
100 se=strel('disk',5);
101 tm2=imdilate(tml,se);
102 tm3=imfill(tm2,'holes');
103 L = bwlabel(tm3);
104 s = regionprops(L, 'Area');
105 area_values=[s.Area];
106 maxarea=max(area_values);
107 idx=find(area_values==maxarea);
108 wingiso = ismember(L, idx);
109 figure, imshow(wingiso), title('wingiso')
110 tm=reshape(tm, size(tm,1)*size(tm,2),1);
111 modetm=mode(tm);
112 LSMout(~wingiso)=modetm;
113 [LLL]=bwlabel(LSMout);
114 t1=imfill(LLL,'holes');
115 [LLLL]=bwlabel(t1);
116 %set background color
117 L1=double(LLLL);
118 tm=reshape(L1, size(L1,1)*size(L1,2),1);
119 modetm=mode(tm);
120 L2=L1;
121 L2(L1==modetm)=max(max(L1))+1;
122 end

```

```

1 function [minlocation,peaks] = multipeaks(Z)
2 % Takes input wing image Z, creates a smoothed PDF and finds locations of
3 % the modes of subdistributions which are known to exist in the wing
4 % image
5 % Inputs: wing image Z
6 % Output: MINLOCATION: pixel intensity value with a the local minimum
7 % of frequency of occurrence between the 2 highest located local PEAKS
8 % PEAKS: the pixel intensity values which are the modes of the image
9 % background subdistribution (highest peak) and the wing cell
10 % subdistribution
11
12 % set desired number of peaks. 2 for wing images
13 numberofpeaks=2;
14 % initiate the locator
15 peaksthresh=70;
16 Z=double(Z);
17 A=reshape(Z, (size(Z,1)*size(Z,2)),1);

```

```

18 %% Fit a distribution using a kernel smoother
19 myFit = fitdist(A, 'kernel');
20 %class(myFit)
21 %% Visualize the resulting fit
22 index = 0:255;
23 % figure, plot(index, pdf(myFit, index)),...
24 % title(sprintf('smoothed probability distribution wing%dBIG',j))
25
26 %% Form an array of probability density at 256 nodes 0:255
27 mydist=pdf(myFit,index)*1000;
28 diffmydist=diff(mydist);
29 peaksArray=[mydist;[0 diffmydist]];
30
31 %% find the input number of peaks
32 threshold=peaksthresh;
33 k=0;
34 peaks=zeros(1,numberofpeaks);
35 while k<numberofpeaks && threshold>2
36     for i=2:255
37         if peaksArray(1,i)> threshold
38             if peaksArray(2,i)>0
39                 if peaksArray(2,i+1)<0
40                     peaks(k+1)=i;
41                     k=k+1;
42                 else
43                     end
44             else
45                 end
46         else
47             end
48     end
49     threshold=threshold-1;
50     if k>=numberofpeaks
51         break
52     else
53         k=0;
54     end
55 end
56
57 % find the minimim between the peaks
58 [Y I]=min(peaksArray(1,peaks(end-1):peaks(end)));
59 minlocation=I+peaks(end-1)-1;
60 end

```

```

1 function [LL, bwth] = processbinaryedgeseg( bw, areathresh,t)
2 %Input is a binary image BW of the vein segmentation
3 imgcomp=imcomplement(bw);
4 %remove the exterior of the wing image from the segmentation result
5 bw1=imclearborder(imgcomp);
6 %label the remaining wing subregions
7 [L]=bwlabel(bw1);
8 %apply an area thresholding to eliminate extraneous data
9 s = regionprops(L, 'Area');
10 area_values = [s.Area];
11 idx = find((area_values>=areathresh));
12 bw2=ismember(L,idx);
13 % label and compute stats of the remaining subregions of interest
14 [LL NN]=bwlabel(bw2);
15 ss=regionprops(LL, 'Area','Centroid','Perimeter');
16 bwthick=bwmorph(LL, 'thicken',t);
17 bwth=bwlabel(bwthick);
18 end

```

```

1 function [cutimage, binaryImage2] = cutpointmasksingleimage(img,k)
2 %CUTPOINTMASK2 returns an output image after a masking procedure by
3 %creating a segmentation boundary line from input cutpoints
4 % INPUT:

```

```

5 % INPUT: k, the image number (eg, k=45, this function reads in
6 % wing45BIG.tif from the \Wings directory).
7 % OUTPUT: the original images after the masking procedure
8
9 % reshape input cutpoints to a 2X2 array [x1 y1; x2 y2]
10 cutpointlist=xlsread('Thesis\cutpoints.xlsx');
11 cutpoints=reshape(cutpointlist(k,:),2,2)';
12 [x1]=cutpoints(1);
13 [y1raw]=cutpoints(3);
14 [x2]=cutpoints(2);
15 [y2raw]=cutpoints(4);
16 %change from pixel coordinates to cartesian coordinates
17 y1=abs(y1raw-1199);
18 y2=abs(y2raw-1199);
19
20 % calculate slope and y-intercept of the line formed from the 2 cutpoints
21 m=(y2-y1)/(x2-x1);
22 b=y2-m*x2;
23 % therefore, y=mx+b (we are in cartesian coordinates)
24 x=0:1600;
25 y=m*x+b;
26 % figure
27 % plot(x,y), axis ([0 1600 0 1200])
28 % these bounds assume starting point in coordinate system is (0,0), not
29 % (1,1)
30 xbound1=(-b/m);
31 xbound2=(1200-b)/m;
32 ybound1=b;
33 ybound2=m*1600+b;
34
35 %determine the intersection of the cutpoint line with the image perimeter
36 if xbound1 <=1600
37     if xbound1>0
38         keeper1=[xbound1 1];
39     else
40         keeper1=[1 ybound1];
41     end
42 else
43     keeper1=[1600 ybound2];
44 end
45
46 if xbound2<=1600
47     if xbound2>0
48         keeper2=[xbound2 1200];
49     else
50         keeper2=[1 ybound1];
51     end
52 else
53     keeper2=[1600 ybound2];
54 end
55 keeper1=uint16(keeper1);
56 keeper2=uint16(keeper2);
57 y1pixel=double(keeper1(2));
58 y2pixel=double(keeper2(2));
59 keeper1(2)=uint16(abs(y1pixel-1199));
60 keeper2(2)=uint16(abs(y2pixel-1199));
61 if keeper1(2)>1190
62     keeper1(2)=1200;
63 else
64     end
65 if keeper2(2)>1190
66     keeper2(2)=1200;
67 else
68     end
69 keeper1=double(keeper1);
70 keeper2=double(keeper2);
71
72 % create a mask from the line
73 kk=num2str(k);
74 underImage=img;
75 burnedImage=zeros(size(underImage));
76 figure

```

```

77 subplot(2, 2, 1);
78 axis ([0 1600 0 1200])
79 imshow(underImage)
80 % Create line mask, h, as an ROI object over the second image in the
81 % bottom row.
82 subplot(2,2,2)
83 axis ([0 1600 0 1200])
84 imshow(underImage)
85 % Second argument defines line endpoints in form [x1 x2] [y1 y2].
86 hLine = imline(gca,[keeper1(1) keeper2(1)], [keeper1(2) keeper2(2)] );
87 axis ([0 1600 0 1200])
88 % Create a mask from the ROI object.
89 binaryImage2 = hLine.createMask();
90 burnedImage(binaryImage2) = 255;
91 bwthick=im2bw(imdilate(burnedImage,strel('line',2,0)));
92 bwthick1=imcomplement(bwthick);
93 bwth=bwlabel(bwthick1);
94 s=regionprops(bwthick1, 'Area');
95 area_values=[s.Area];
96 maxarea=max(area_values);
97 idx=find(area_values==maxarea);
98 cutpointmask = ismember(bwth, idx);
99 cutimage=underImage;
100 cutimage(imcomplement(cutpointmask))=0;
101 end

```

```

1 function [U,S,V, E95, E99, imgmatrix, AvgWing] = MakeSVD(imagematrix )
2 %INPUT: A matrix in which each column is a wing image reshaped as a vector
3 % OUTPUTS: U: left singular vectors of (after mean-centering) IMAGEMATRIX
4 % S: singular values of IMAGEMATRIX
5 % V: right singular vectors..
6 % ENERGY95: number of PCs to retain 95% variance
7 % ENERGY99: ... to retain 99% variance
8 % IMGMATRIX: mean centered IMAGEMATRIX
9 % AvgWing: the average wing image over the set
10
11 %compute the mean face by averaging over each row
12 AverageWing=mean(imagematrix ,2);
13 [r, c]=size(imagematrix);
14 % subtract the mean face from each image to create zero mean rows
15 imgmatrix=imgmatrix-repmat(AverageWing,[1,c]);
16 % produces the economy size svd
17 [U,S,V] = svd(imgmatrix ,0);
18 %determine the number the eigenvectors to keep to contain
19 %the threshold amount of energy
20 Threshold1=.95;
21 Threshold2=.99;
22 SingularValueEnergy=diag(S).^2;
23 KeepEnergy = cumsum( SingularValueEnergy )/sum( SingularValueEnergy ) ;
24 E95 = find( KeepEnergy > Threshold1,1 );
25 E99 = find( KeepEnergy > Threshold2,1 );
26 end

```

## BIBLIOGRAPHY

## BIBLIOGRAPHY

- [1] R. Mitchum, “Fruit flies’ genetic wealth has scientists abuzz.” <http://www.phys.org/news155751263.html/>, Mar 2009.
- [2] A. Carter, E. Osborne, and D. Houle, “Heritability of directional asymmetry in drosophila melanogaster,” *International Journal of Evolutionary Biology*, vol. 2009, pp. 1–7, 2009.
- [3] C. Plabon, T. F. Hansen, A. Carter, and D. Houle, “Evolution of variation and variability under fluctuating, stabilizing, and disruptive selection,” *Evolution*, vol. 64, no. 7, pp. 1912–1925, 2010.
- [4] D. Houle, J. Mezey, P. Galpern, and A. Carter, “Automated measurement of drosophila wings,” *BMC Evolutionary Biology*, vol. 3, December 2003.
- [5] R. Gonzalez, R. Woods, and S. Eddins, *Digital Image Processing Using MATLAB*. Tata McGraw-Hill Education Private Limited, 2nd ed., 2010.
- [6] K. Birdsall, E. Zimmerman, K. Teeter, and G. Gibson, “Genetic variation for the positioning of wing veins in drosophila melanogaster,” *Evolution & Development*, vol. 2, no. 1, pp. 16–24, 2000.
- [7] D. Houle, *The WINGMACHINE: Drosophila wing splining and editing with Wings and CPReader*, 2009.
- [8] M. Bhatia, D. Yadav, Madhurima, P. Gupta, G. Kaur, J. Singh, M. Gandhi, and A. Singh, “Implementing edge detection for medical diagnosis of a bone in matlab,” in *Computational Intelligence and Communication Networks (CICN), 2013 5th International Conference on*, pp. 270–274, Sept 2013.
- [9] L. Florack, B. Romeny, J. Koenderink, and M. Viergever, “Scale and the differential structure of images,” *Image and Vision Computing*, vol. 10, pp. 376–388, 1992.
- [10] J.-M. Chang, N. Huynh, M. Vazquez, and C. Salafia, “Vessel enhancement with multiscale and curvilinear filter matching for placenta images,” in *Systems, Signals and Image Processing (IWSSIP), 2013 20th International Conference on*, pp. 125–128, July 2013.
- [11] A. Pressley, *Elementary Differential Geometry*. Springer, 2001.
- [12] A. Frangi, W. Niessen, K. Vincken, and M. Viergever, “Multiscale vessel enhancement filtering,” in *Medical Image Computing and Computer-Assisted Intervention MICCAI98* (W. Wells, A. Colchester, and S. Delp, eds.), vol. 1496 of *Lecture Notes in Computer Science*, pp. 130–137, Springer Berlin Heidelberg, 1998.

- [13] S. Osher and J. Sethian, “Fronts propagating with curvature-dependent speed: algorithms based on hamilton–jacobi formulations,” *Journal of Computational Physics*, vol. 79, no. 1, pp. 12–49, 1988.
- [14] S. Osher and R. Fedkiw, *Level Set Methods and Dynamic Implicit Surfaces*. Springer-Verlag New York, 2003.
- [15] J. Sethian, *Level Set Methods and Fast Marching Methods*. Cambridge University Press, 2nd ed., 1999.
- [16] S. Osher and C.-W. Shu, “High–order essentially nonoscillatory schemes for hamilton-jacobi equations,” *SIAM Journal on Numerical Analysis*, vol. 28, no. 4, pp. 907–922, 1991.
- [17] Y. Peng, A. Ganesh, J. Wright, W. Xu, and Y. Ma, “Rasl: Robust alignment by sparse and low-rank decomposition for linearly correlated images,” in *Computer Vision and Pattern Recognition (CVPR), 2010 IEEE Conference on*, pp. 763–770, June 2010.
- [18] Mathworks, “Align multiple scenes into a single image using image registration.” <http://www.mathworks.com/discovery/image-registration.html/>.
- [19] G. H. Golub and C. F. Van Loan, *Matrix Computations (3rd Ed.)*. Baltimore, MD, USA: Johns Hopkins University Press, 1996.
- [20] J. Kopf and D. Lischinski, “Depixelizing pixel art,” *ACM Transactions on Graphics (Proceedings of SIGGRAPH 2011)*, vol. 30, no. 4, pp. 99:1 – 99:8, 2011.
- [21] D. Houle, K. van der Linde, and E. Marquez, *Wings 4 and CPR: Curve finding, fitting*, 2014.